Factors generating turbulence in the nocturnal boundary layer

(looking for all kinds of low-level jets)

Joan Cuxart
University of the Balearic Islands

Zagreb, 24 February 2010

1. Windy NBL (steady state, homogeneous)
2. NBL in weak pressure gradients (evolutive, homogeneous)
3. NBL over complex terrain (evolutive, heterogeneous)
4. Small scale motions (random, but not really)

Basic equations

Equations of the atmosphere for any variable (χ):

Local change + advection= forcing terms + turbulence

$$\frac{\partial \chi}{\partial t} + u_i \frac{\partial \chi}{\partial x_i} = F_i - \frac{\partial \overline{u_i' \chi'}}{\partial x_i}$$

(Local Change + Advection= Forcing Terms + Turbulence)

Forcing Terms for Momentum: Coriolis, pressure, viscosity
Forcing terms for Temperature: Radiation, Phase Changes, thermal diffusivity

*Dimensionality of the problem: 1D vs 3D; time and length scales
*Hydrostatic: $w = 0$
*Spatial Homogeneity: $(\frac{\partial}{\partial x} = \frac{\partial}{\partial y} = 0)$ $\Rightarrow \frac{\partial \chi}{\partial t} = F_i - \frac{\partial \overline{w' \chi'}}{\partial z}$
*Stationarity: $(\frac{\partial}{\partial t} = 0)$ $\Rightarrow 0 = F_i - \frac{\partial \overline{w' \chi'}}{\partial z}$
*Free atmosphere: equilibrium between Coriolis and pressure forces: Geostrophic wind

$$u_g = -\frac{1}{\rho f} \frac{\partial p}{\partial y}; v_g = \frac{1}{\rho f} \frac{\partial p}{\partial x} \qquad (2$$

The Ekman layer

In the BL, writing $\overline{w\chi} = -K_\chi \frac{\partial \chi}{\partial z}$

$$0 = f(v - v_g) - -\frac{\partial \overline{w'u'}}{\partial z};\ 0 = -f(u - u_g) - -\frac{\partial \overline{w'v'}}{\partial z}$$

If $\overline{wu} = -K_M \frac{\partial u}{\partial z}$, K_M constant, $v_g = 0$), $a = \sqrt{\frac{f}{2K}}$:

$$\begin{aligned} u &= u_g(1 - exp(-az)cos(az)) \\ v &= u_g exp(-az)sin(az) \end{aligned}$$

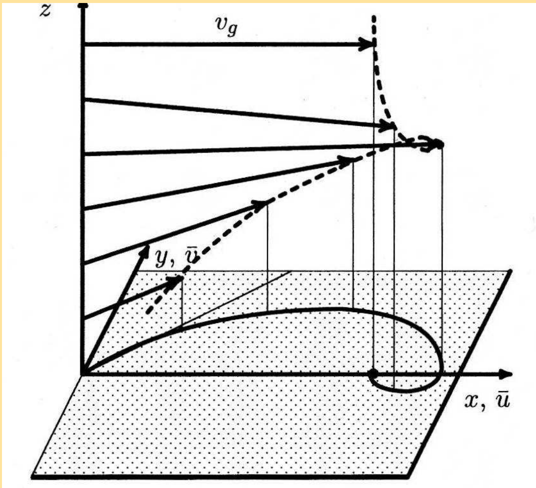

The stably stratified case - Garratt (1992)

$\xi = z/h_e; h_e = 0.37\sqrt{u_{*0}L/f}$

$$\frac{V - V_g}{V_g} = exp(-i\pi/3)(1-\xi)^{(1+i\sqrt{3})/2}$$

$$\frac{\theta_v - \theta_{v0}}{\theta_{v0*}} = -(h_e/L)(Ri/k/Rf^2)ln(1-\xi)$$

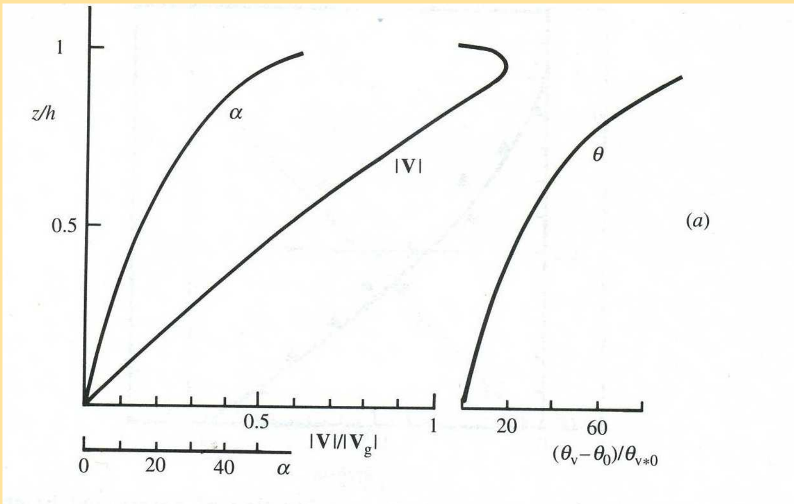

(Nieuwstadt 1985)

$$\frac{\overline{w\theta}}{\overline{w\theta_0}} = 1 - \xi; \; \frac{|\tau|}{\rho u_{0*}^2} = (1 - \xi)^{3/2}$$

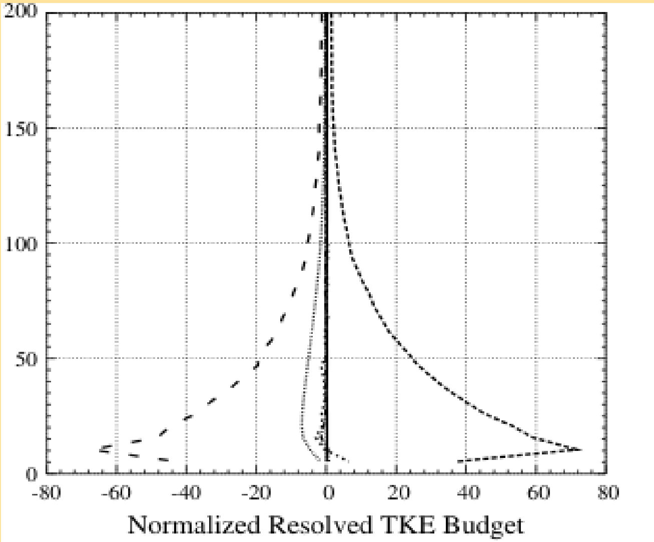

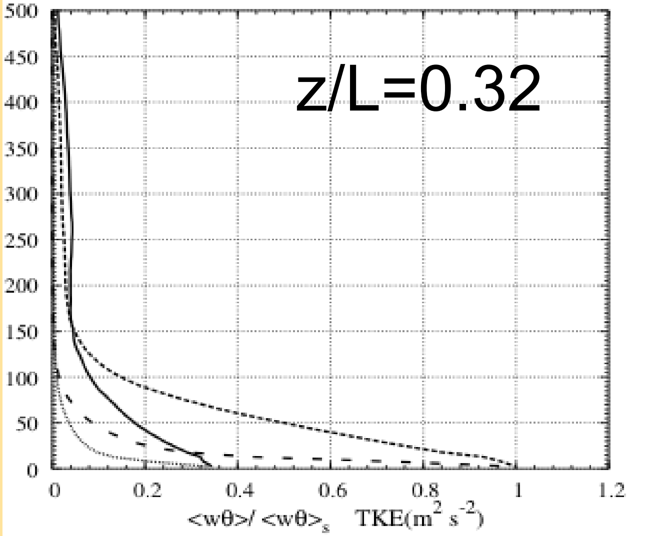

(Jimenez/Cuxart 05)

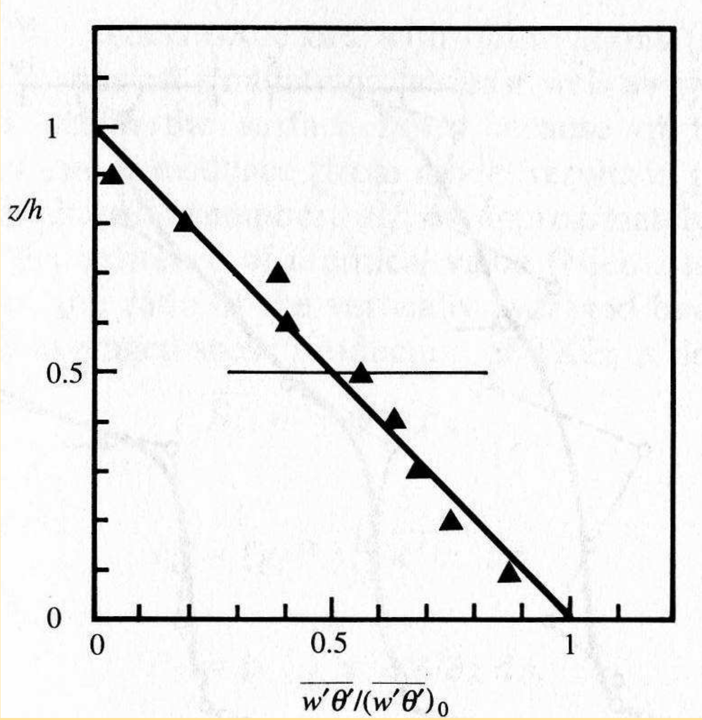

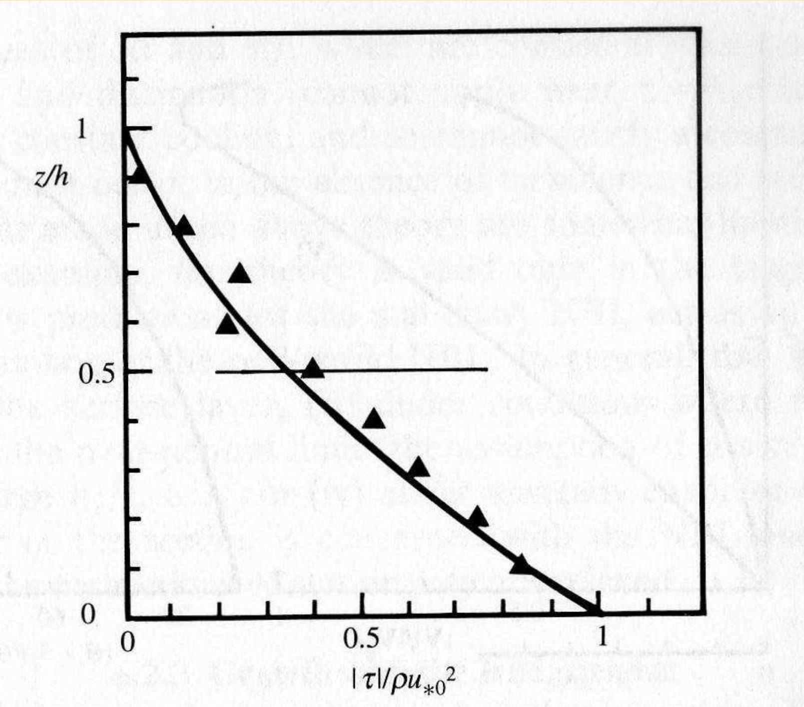

And a theoretical relation between external factors and the heat flux exists (Derbyshire 1990)

$$\frac{g}{\theta_0}\overline{w\theta_0} = -V_g^2 f\ Rf/\sqrt{3} \tag{9}$$

Given R_f, the upper limit of the heat flux depends only on external factors V_g and f

For $V_g = 10m/s, f = 10^{-4}, Rf = 0.2, \overline{w'\theta'_0} = -40W/m^2$

Case 8 m/s

Max flux: 0.024 K m/s

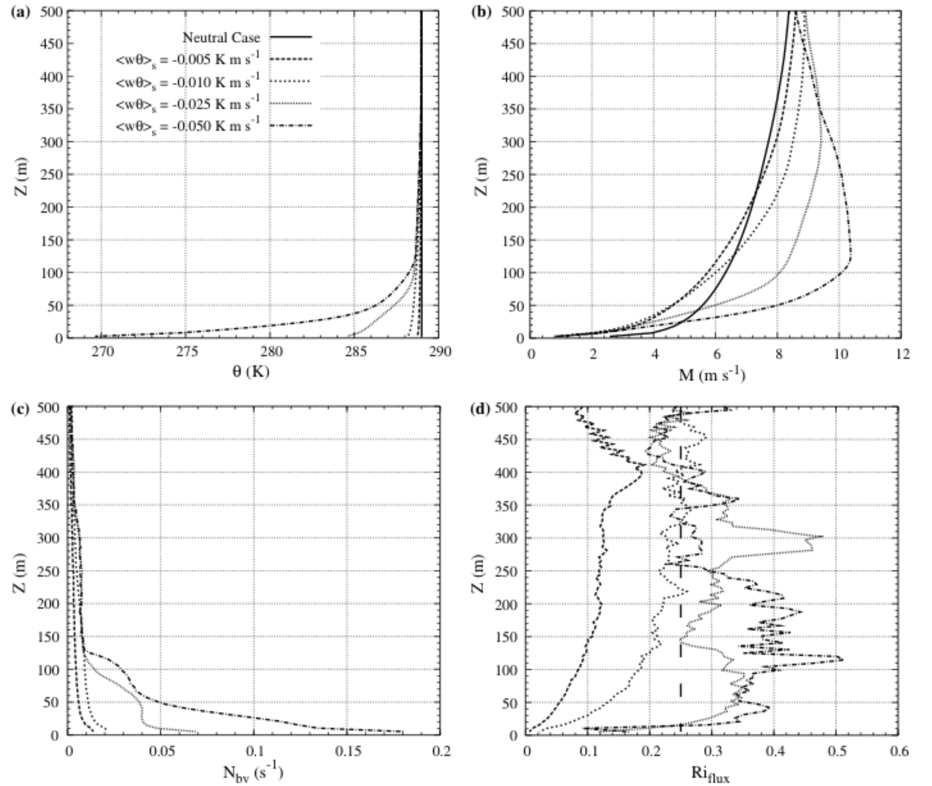

Figure 2. Mean values for $G = 8\,\mathrm{m\,s^{-1}}$ as the surface cooling increases. (a) Potential temperature, (b) Wind speed, (c) Brunt–Väisälä frequency, (d) Flux Richardson number.

(Jimenez/Cuxart 05)

$$(kz/u_{*0})\partial U/\partial z = \phi_M(\xi)$$

$$(kz/\theta_{v*0})\partial\theta_v/\partial z = \phi_H(\xi)$$

$$\phi_M = \phi_H = 1 - \beta\xi; \quad \beta \approx 5$$

Surface Layer

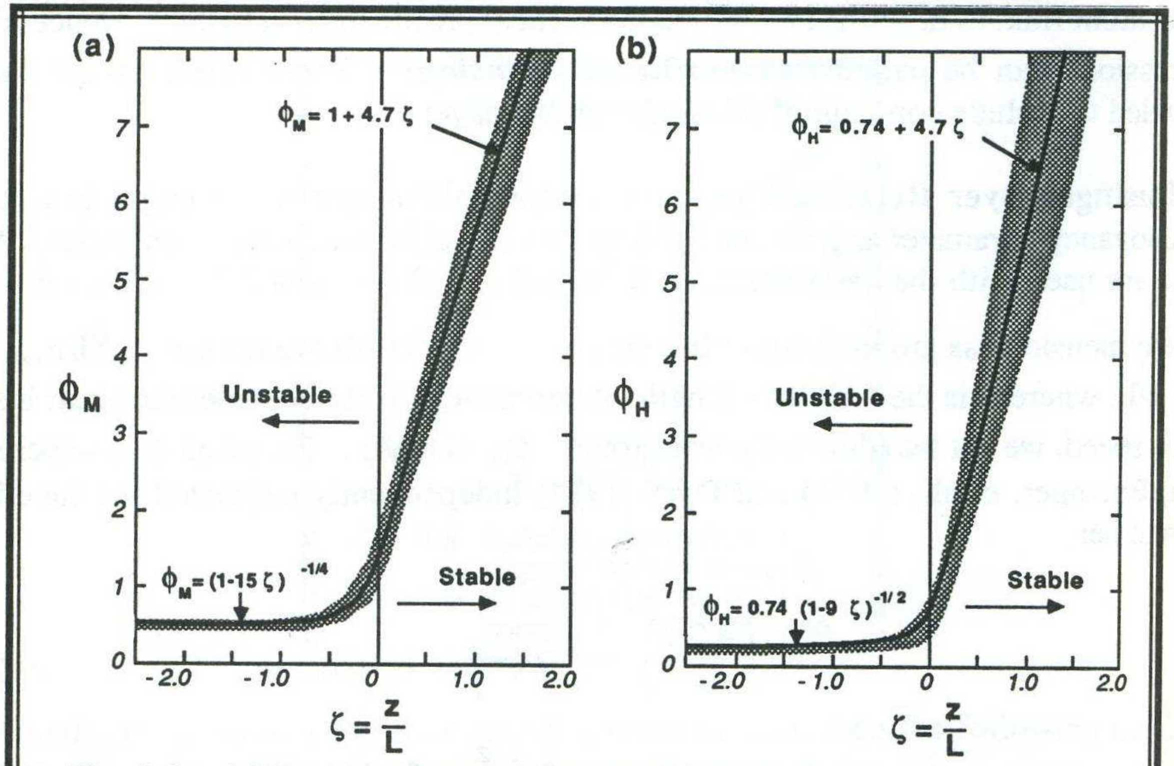

Fig. 9.9 (a) Range of dimensionless wind shear observations in the surface layer, plotted with interpolation formulas. (b) Range of dimensionless temperature gradient observations in the surface layer, plotted with interpolation formulas. After Businger, et al. (1971).

Height of the NBL

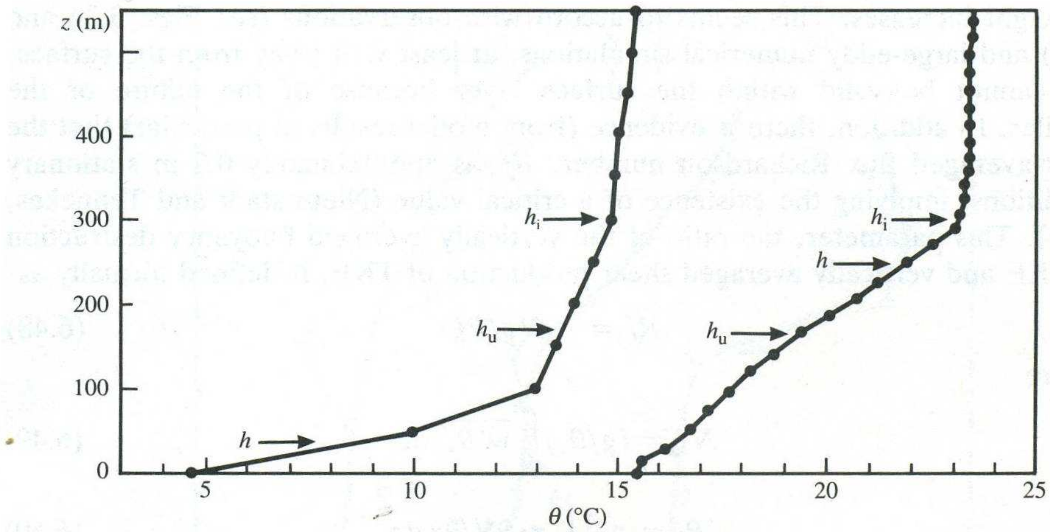

Fig. 6.11 Sample θ profiles under clear sky, night-time conditions from the WANGARA (left) and VOVES (right) experiments. Arrows indicate the respective heights of the surface inversion (h_i), low-level wind maximum (h_u) and NBL (h). After André and Mahrt (1982), *Journal of Atmospheric Sciences*, American Meteorological Society.

3 options:

* Height of the surface inversion (hi):
  can rise 20 m/h and reach several hundred meters
* Location of the wind maximum (hu):
  near-top of the Ekman like spiral
* Depth of the turbulent layer (h):
  layer with sustained turbulence generated by wind shear

A composite profile

Ri = -BP/DP

K= -<w'T'> (∂T/∂z)

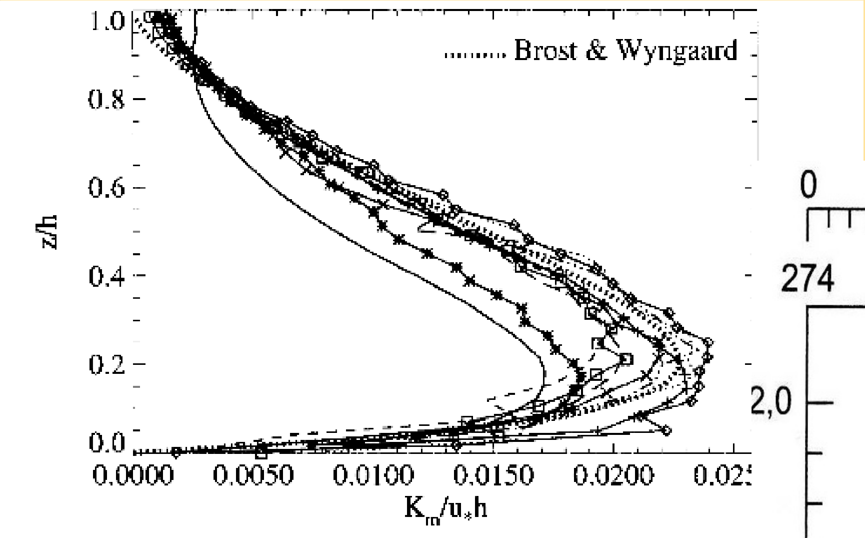

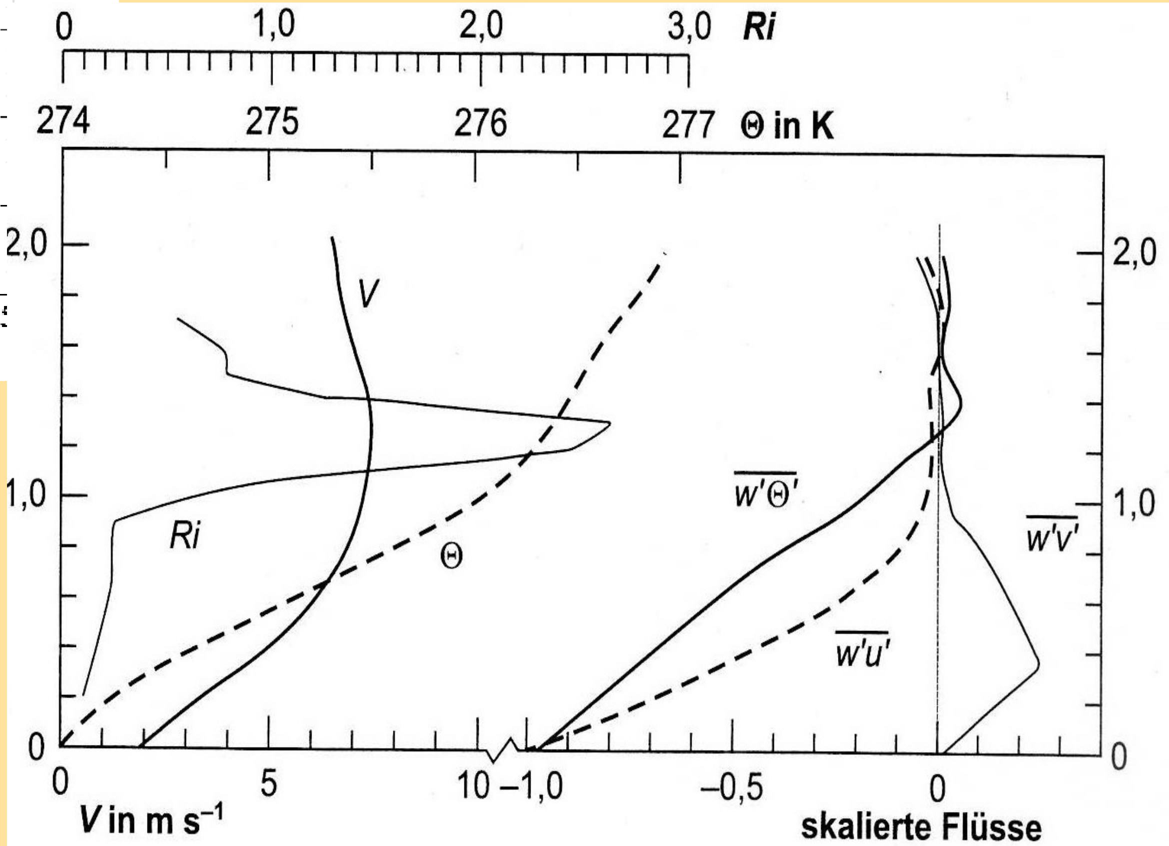

Intermittency regime

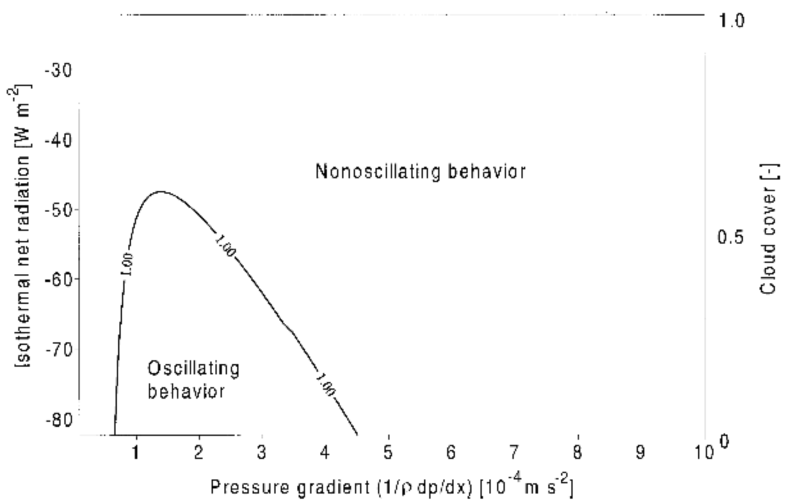

FIG. 4. Contour plot showing the dependence of the dimensionless intermittency parameter Π on the isothermal net radiation and on the pressure gradient. The critical level $\Pi = 1$ is given in a single contour line. For convenience, the cloud cover corresponding to the isothermal net radiation values is given on the right axis.

No jet considered
Budget equations in the surface layer
Ct pressure gradient and h
Radiation

Van de Wiel et al (2002)

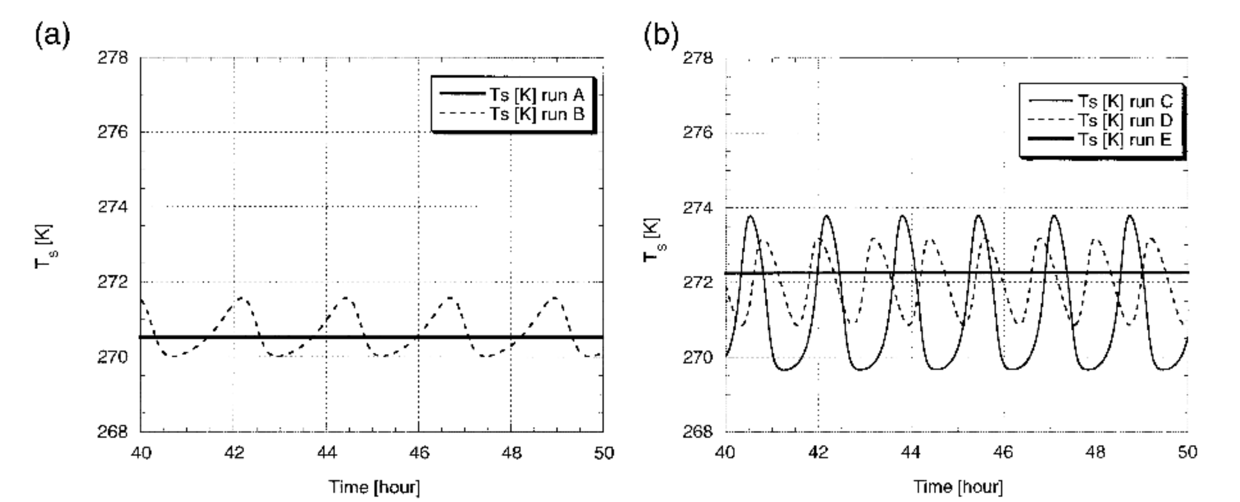

NBL Spectra: waves and turbulence

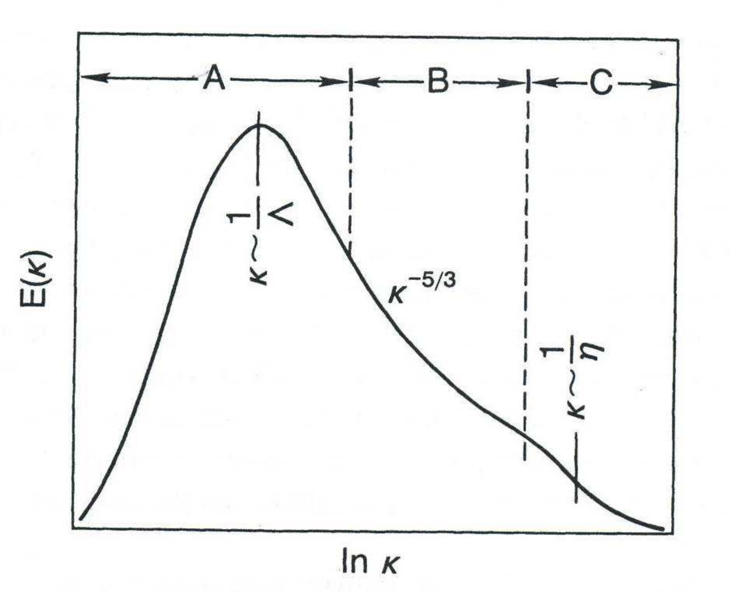

$N_{BV} = \sqrt{\frac{g}{\theta_v}\frac{\partial \theta_v}{\partial z}}$, $l_B = \sigma_w / N_{BV}$ (100-200 m for weakly stable, 1m for strongly stable)

Time scales: $\tau_R = h/0.01u_*$ order of several to more than 10 hours

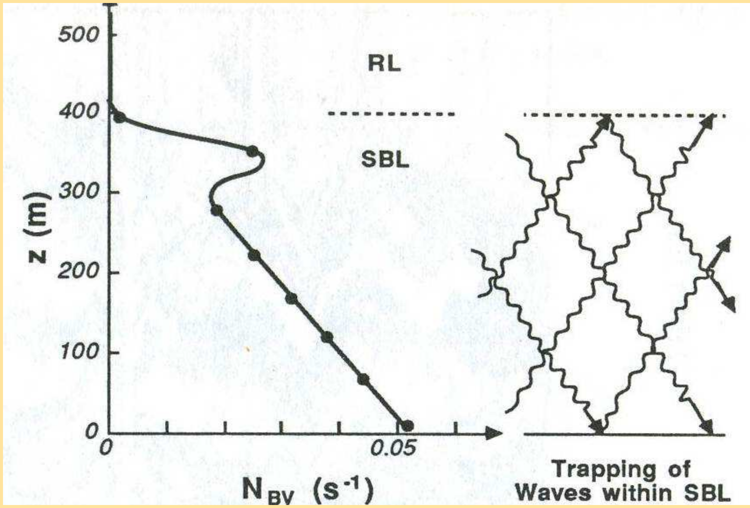

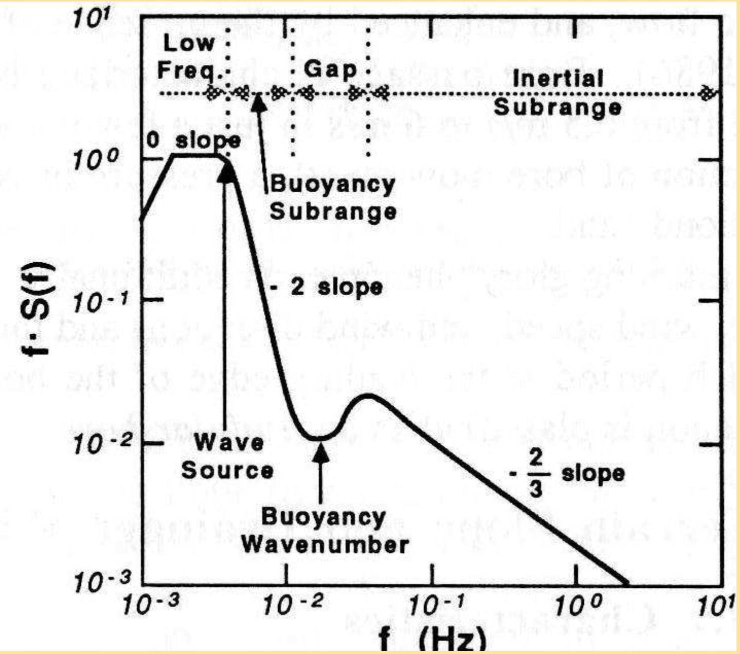

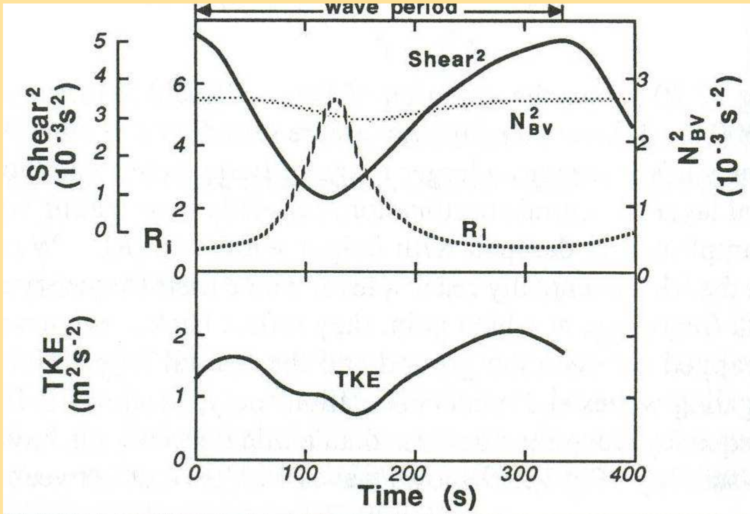

Locally flat, mountains far away

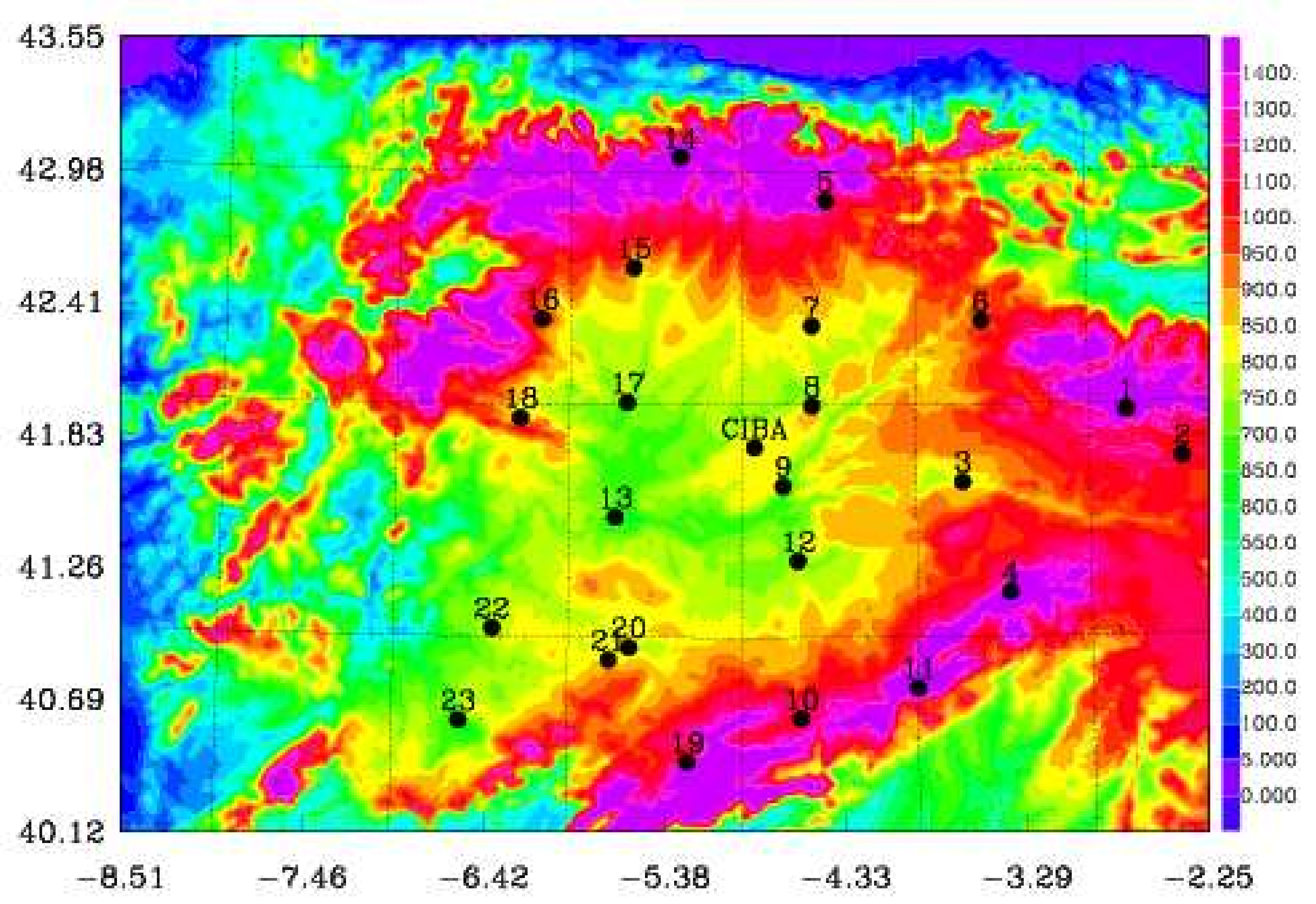

Inertial oscillations

Undamped

$$\frac{\partial u}{\partial t} = f(v - v_g);\ \frac{\partial v}{\partial t} = -f(u - u_g)$$

$$V_{ag} = V - V_g;\ \frac{\partial V_{ag}}{\partial t} = -ifV_{ag};\ V_{ag} = V^i_{ag}exp(-ift)$$

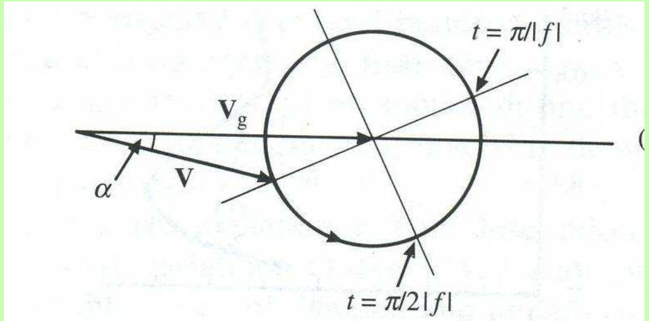

Governed by the inertial period $T = 2\pi/f = \pi/\Omega sin\varphi = 12h/sin\varphi$;

$\phi(^\circ)$	0	30	40	50	60	90
T (h)	∞	24	18.7	15.7	13.9	12.0

For $\varphi = 40^\circ$, maximum wind occurs for $\pi/2 < ft < \pi$ (6h)

Damped

In the turbulent NBL (if ug.ne.0, vg=0)

$$\frac{\partial V}{\partial t} = -if(V - u_g) - \tau_0/\rho h$$

Taking $\tau_0 = \rho k_s V$, and $v_g = 0$

$$V^L = \frac{if}{ks/h + if}u_g + A^L exp[-(if + k_s/h)t]$$

$$V^U = u_g + A^U exp(-ift)$$

(Thorpe and Guymer 77)

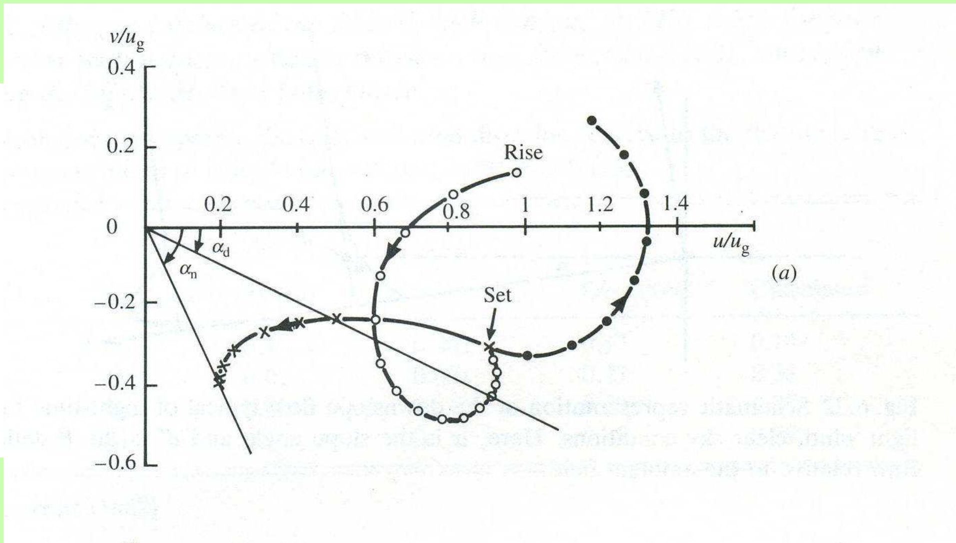

Generation of a strong directional shear layer

A classical windy NBL night

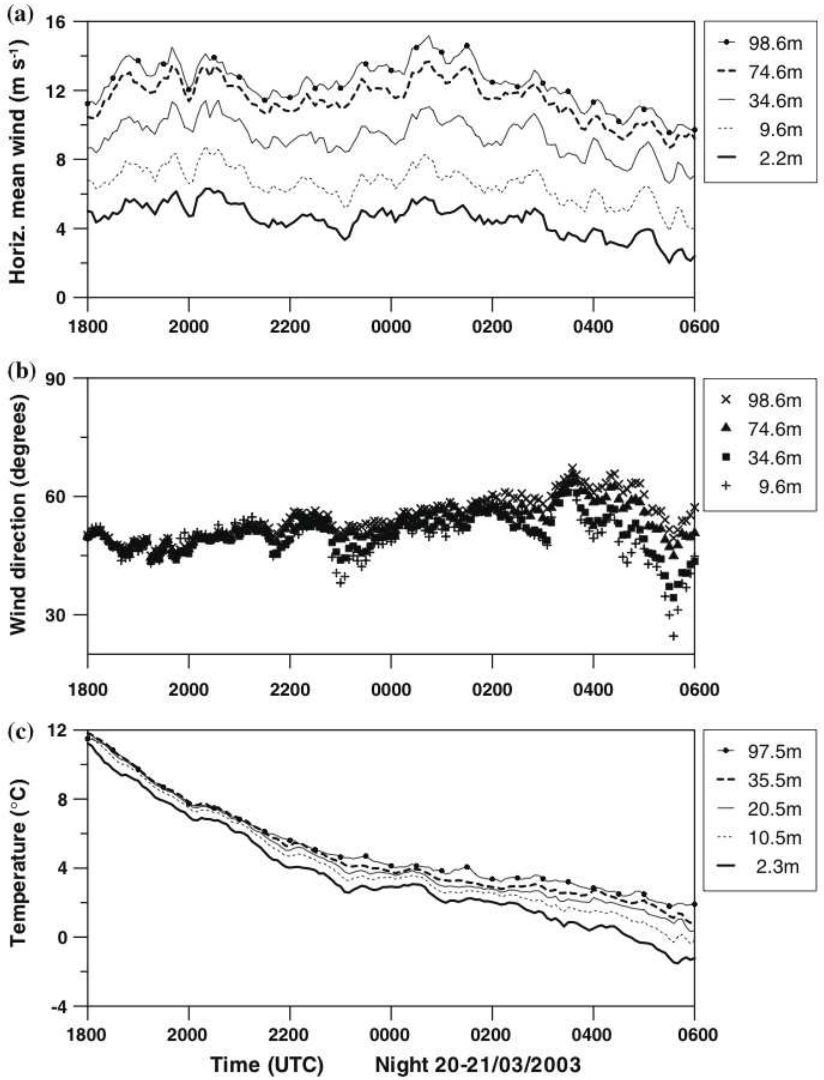

Fig. 5 Time series (using 5-min averaged data) of (**a**) horizontal mean wind, (**b**) wind direction, (**c**) temperature, (**d**) local stability parameter z/Λ, (**e**) vertical heat flux and (**f**) turbulence kinetic energy, at several heights above the ground, for the night 20–21 March 2003

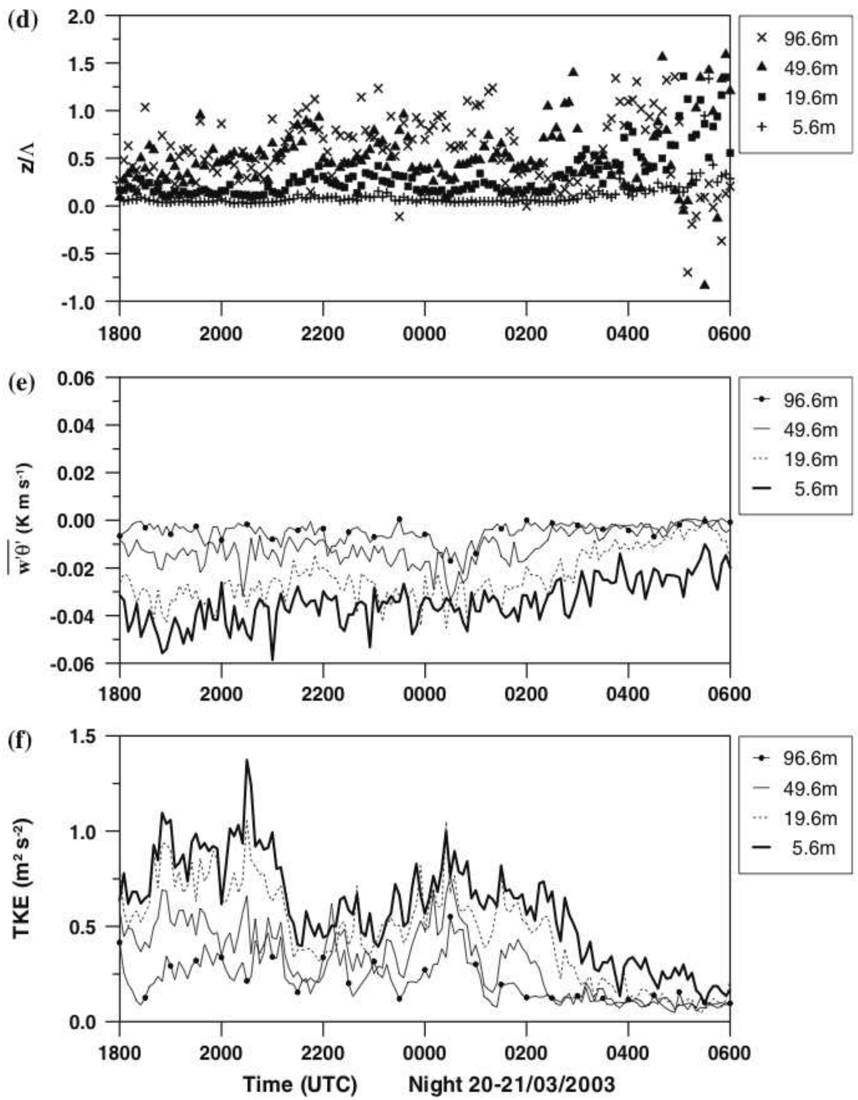

Fig. 5 continued

(Conangla et al 08)

A strongly stratified night

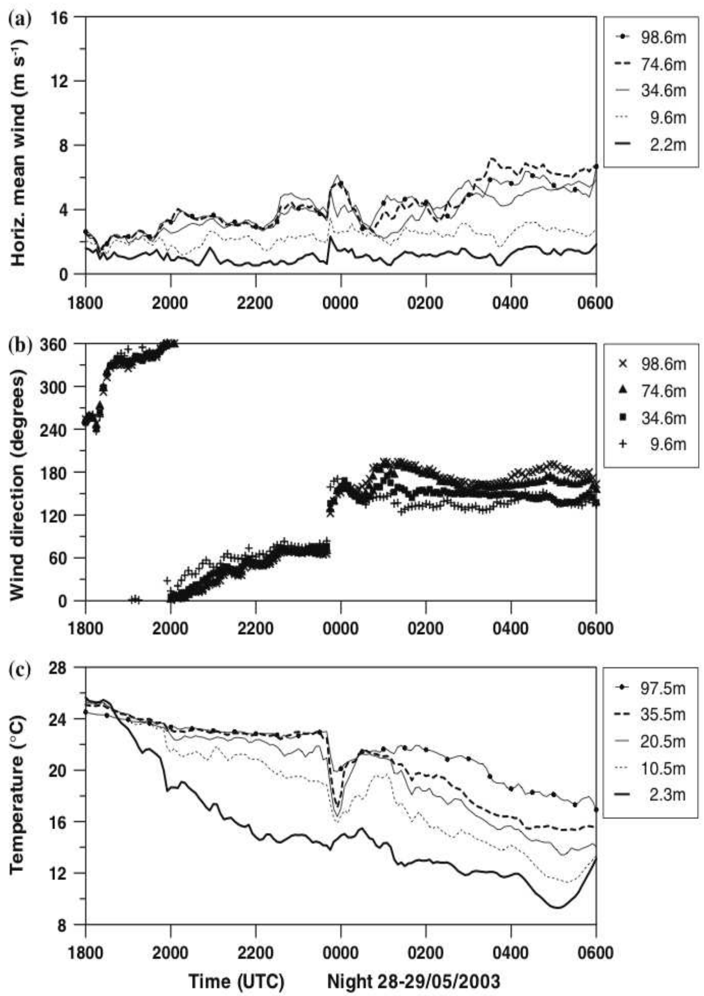

Fig. 6 (a–f) The same as in Fig. 5 for the night 28–29 May 2003. (g) Zoom of (e). (h) Zoom of (f)

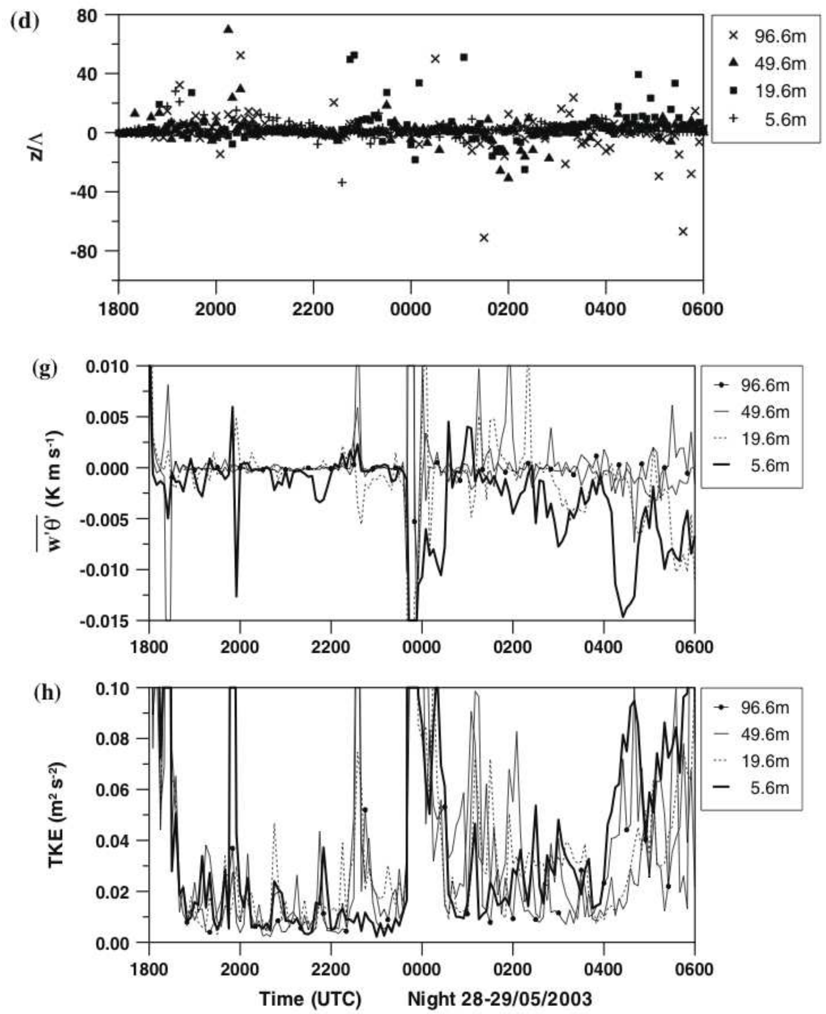

Fig. 6 continued

(Conangla et al 2008)

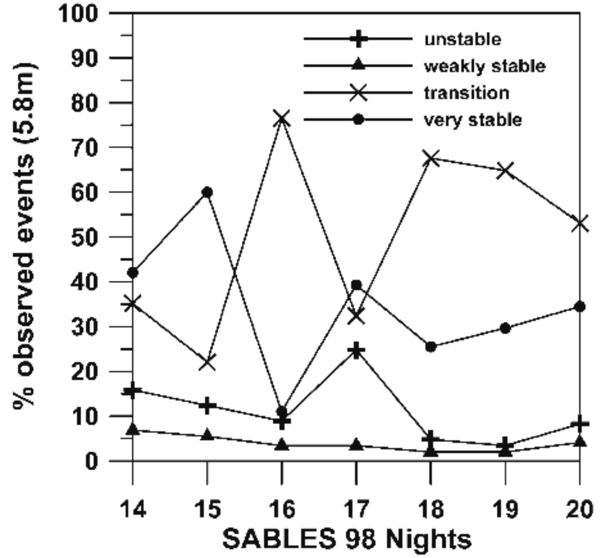

Figure 2. Proportion of each stability type, for the period 14–20 September 1998 during the SABLES 98 campaign, at a height of 5.8 m.

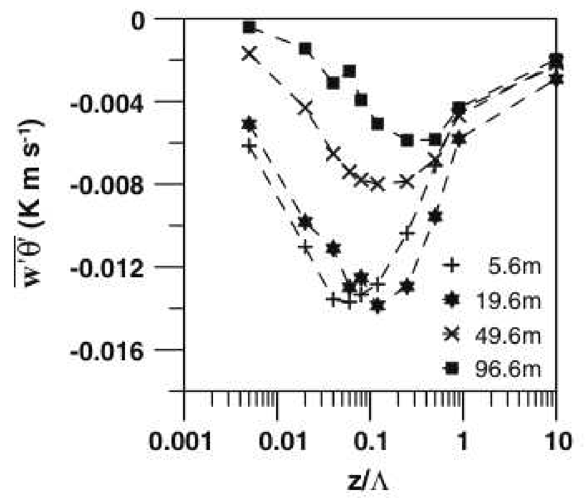

TABLE II

(a) Percentages at which the measurement of turbulence kinematic heat flux ($-\overline{w'\theta'}$) is larger for every recording height. (b) Same as (a) except for turbulence kinetic energy.

(a) Maximum wind at:	Maximum kinematic heat flux ($-\overline{w'\theta'}$) is at height of:			
	5.6 m	19.6 m	49.6 m	96.6 m
34.6 m	66.6	18.2	6.1	9.1
49.6 m	49.4	43.8	0.0	6.8
74.6 m	48.4	32.2	9.7	9.7
(b) Maximum wind at:	**Maximum TKE is at height of:**			
	5.6 m	19.6 m	49.6 m	96.6 m
34.6 m	33.3	21.2	18.2	27.3
49.6 m	21.3	38.2	9.0	31.5
74.6 m	38.7	9.7	12.9	38.7

30-min average data were used, from the 100-m CIBA tower during the period September 2002 to June 2003, when a wind maximum at 34.6 m, 49.6 m or 74.6 m was detected.

(Conangla/Cuxart 06)

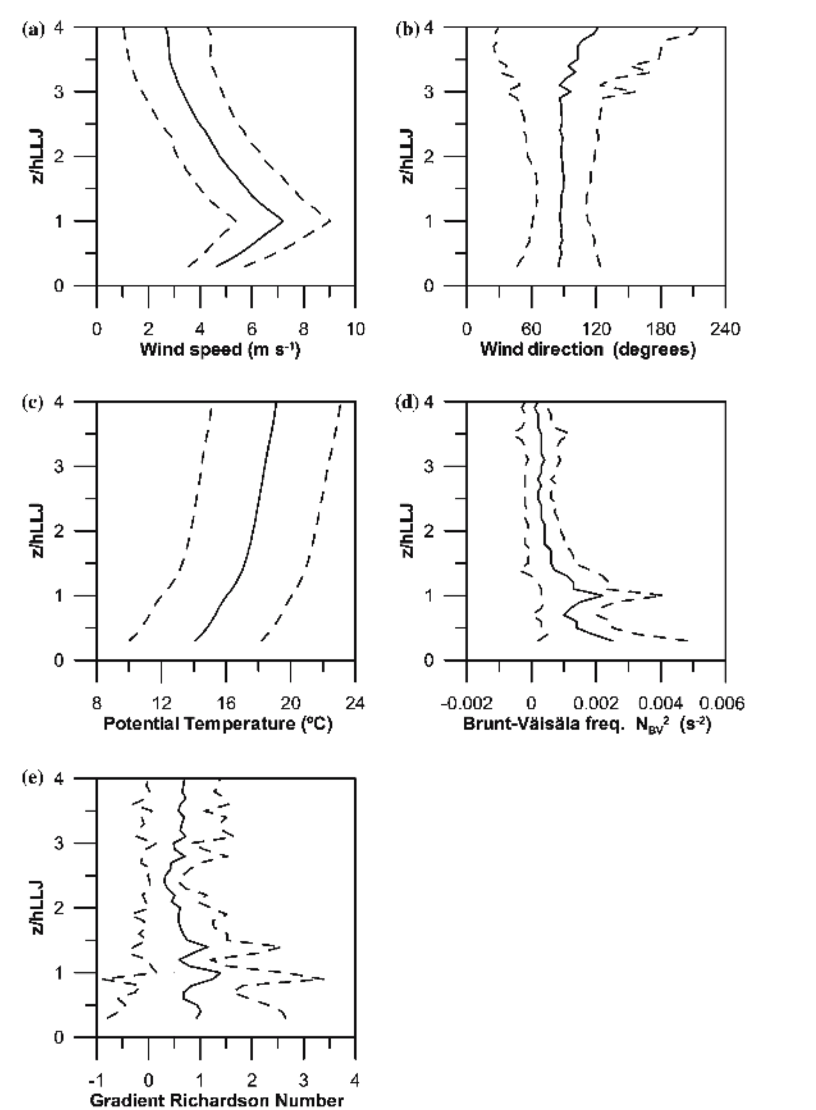

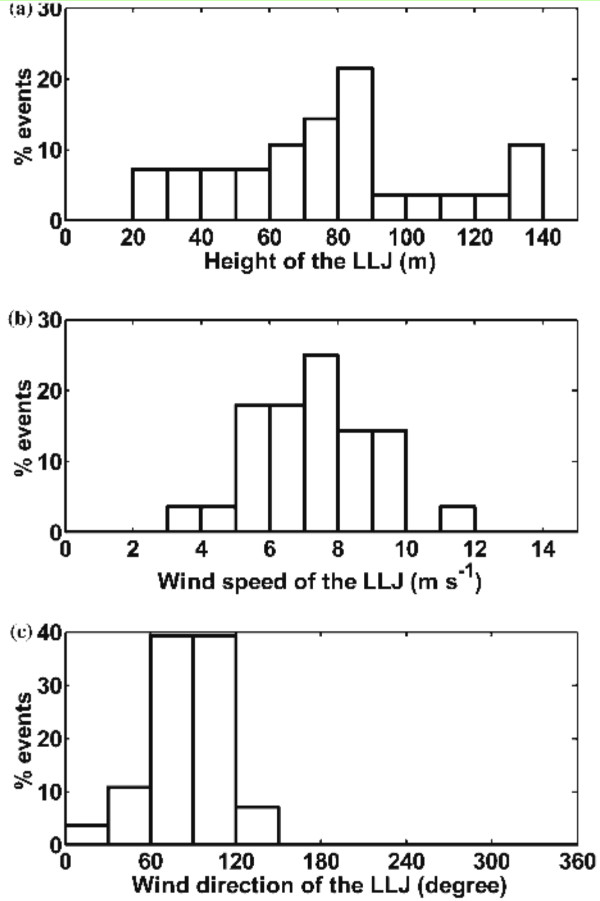

Figure 4. Histograms of height (a), speed (b) and direction (c) of the wind maxima. Data obtained from the selected LLJ profiles, of the balloon soundings made at CIBA during SABLES 98. Percentage of occurrences in each x-bin is shown along the vertical axis.

(Conangla/Cuxart 06)

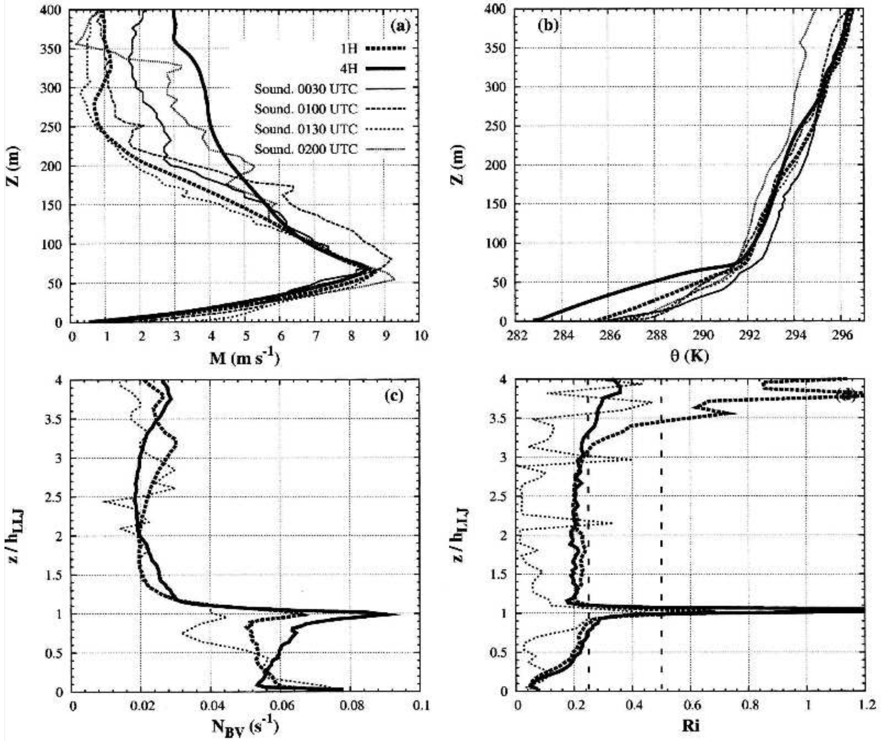

FIG. 2. Half-hourly averaged LES outputs at 1 h (thick continuous line) and 4 h (thick dashed line) and some soundings (thin lines) for (a) wind speed; (b) potential temperature; (c) Brunt–Väisälä frequency; and (d) gradient Richardson number. In (c), (d) only the 0130 UTC sounding is plotted and the y axis is normalized by the LLJ height (h_{LLJ}).

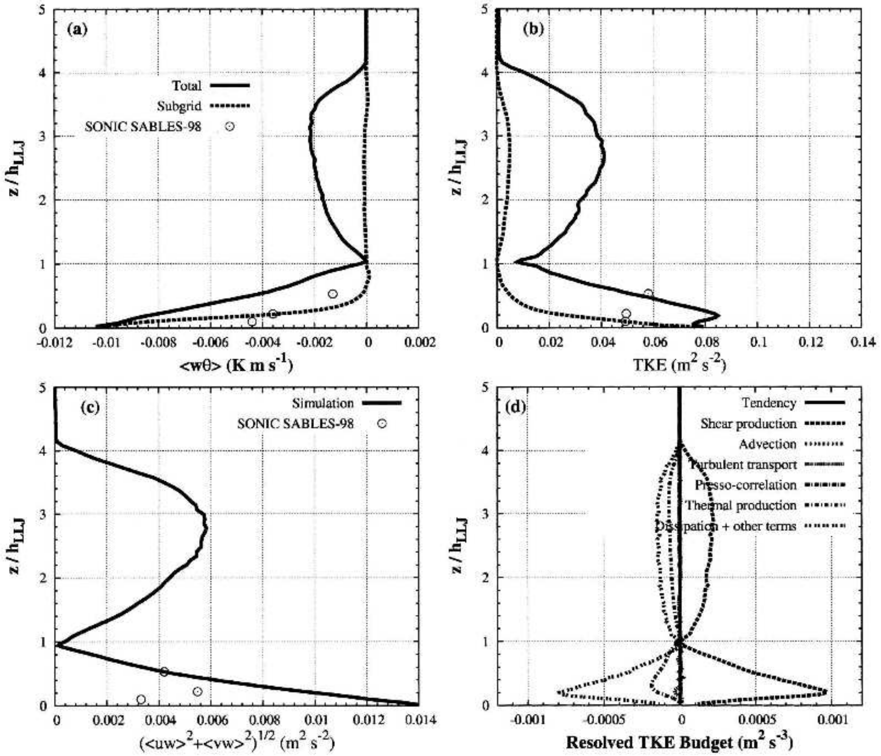

FIG. 3. Averaged LES outputs at 4 h: (a) heat flux; (b) TKE; (c) horizontal part of the Reynolds tensor; and (d) resolved TKE budget. The symbols in (a)–(c) are averages from sonic anemometers. The y axis is normalized by the LLJ height (h_{LLJ}).

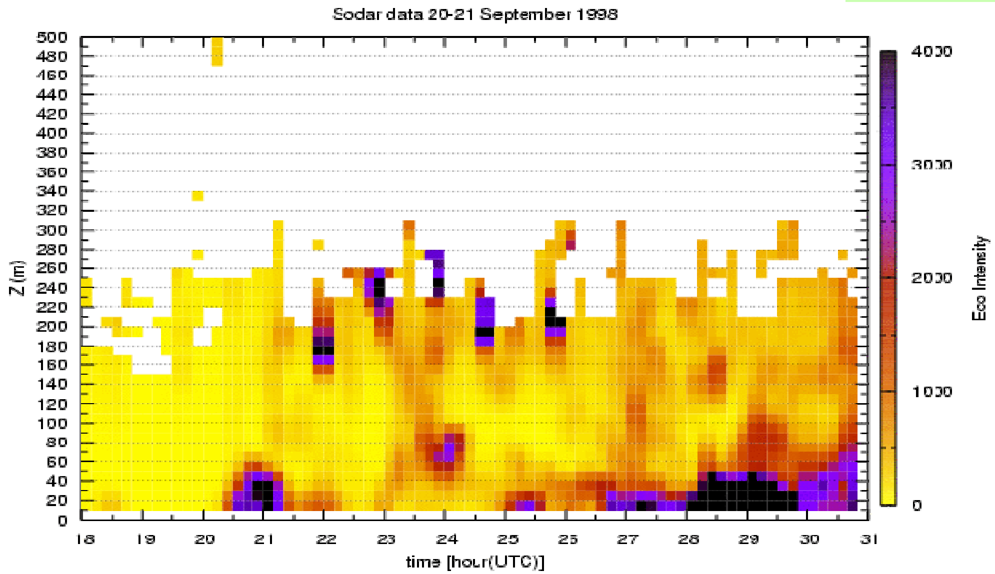

LLJ: an LES simulation

(Cuxart/Jimenez 07)

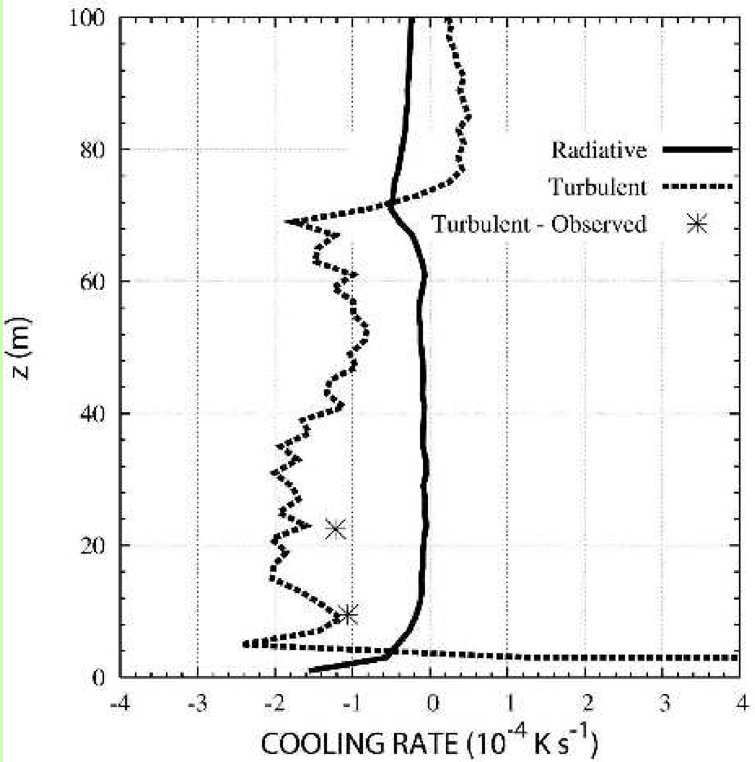

FIG. 1. Radiative $[(1/\rho C_p)(dR_{net}/dz)]$ and turbulent $(d\langle w\theta\rangle/dz)$ coolings computed from the LES (in lines) and from the observations (points) between 0000 and 0200 UTC.

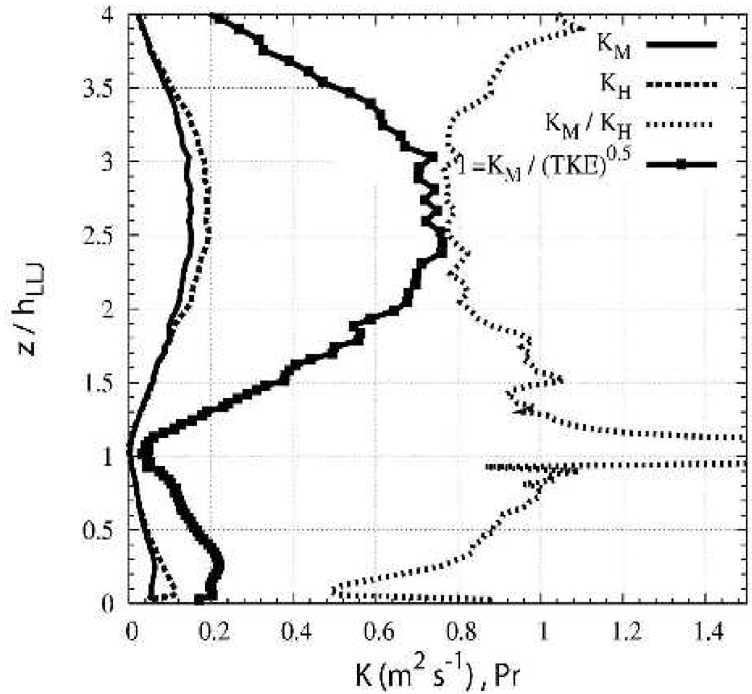

FIG. 10. Eddy diffusivities for heat and momentum (K_H, K_M), turbulence Prandtl number, and mixing length averaged during the fourth hour of the simulation. The y axis is normalized by the LLJ height (h_{LLJ}).

(Cuxart/Jimenez 07)

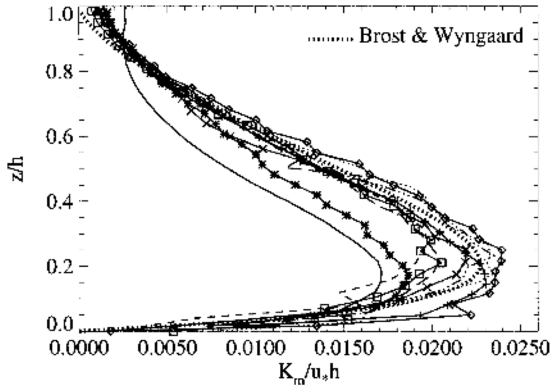

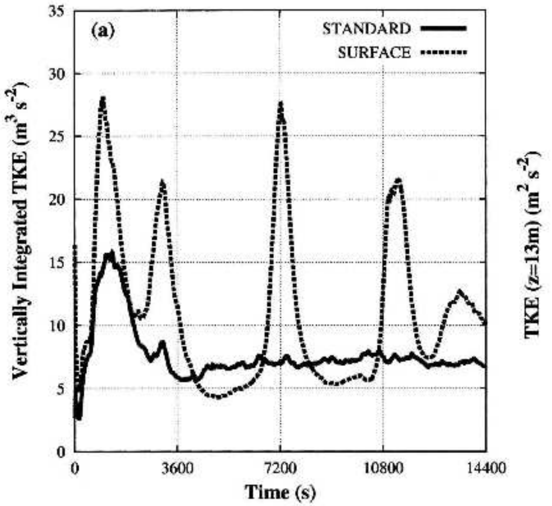

FIG. 6. (a) Vertically integrated TKE time series computec
caption Fig. 5). (b) Time series of the TKE at 13 m computed
the tower between 2100 and 0100 UTC.

(Cuxart/Jimenez 07)

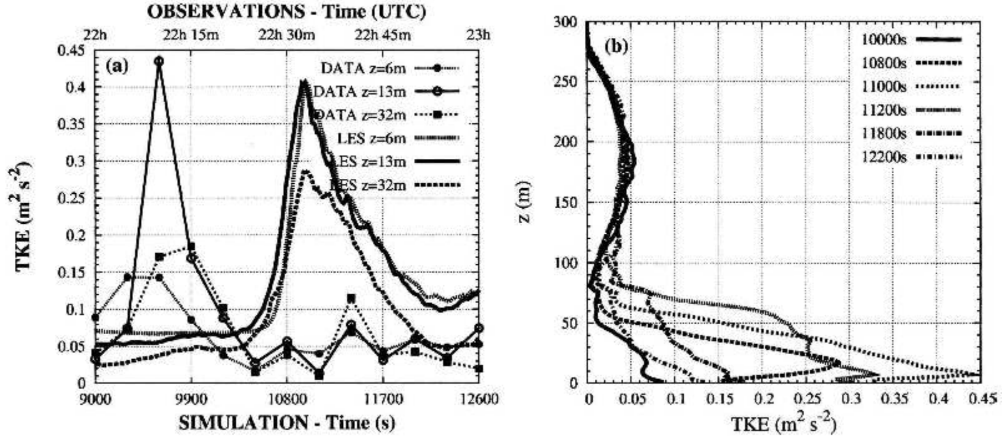

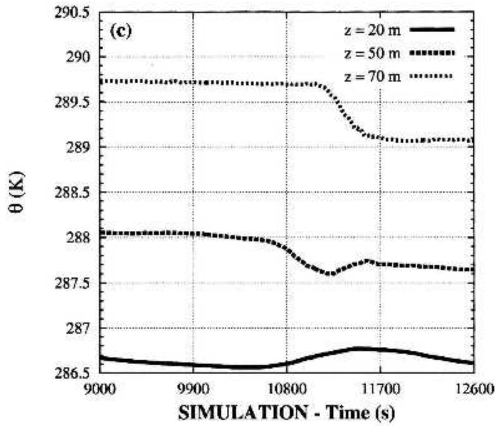

FIG. 7. Results obtained from the surface-forced case. (a) Time series of the TKE at three different levels (6, 13, and 32 m) computed from the LES during the last hour of the run and those measured from the tower between 2200 and 2300 UTC; (b) TKE vertical profiles at different instants during the last hour of the run; and (c) time series of the temperature at different heights (20, 50, and 70 m) during the last hour of the run.

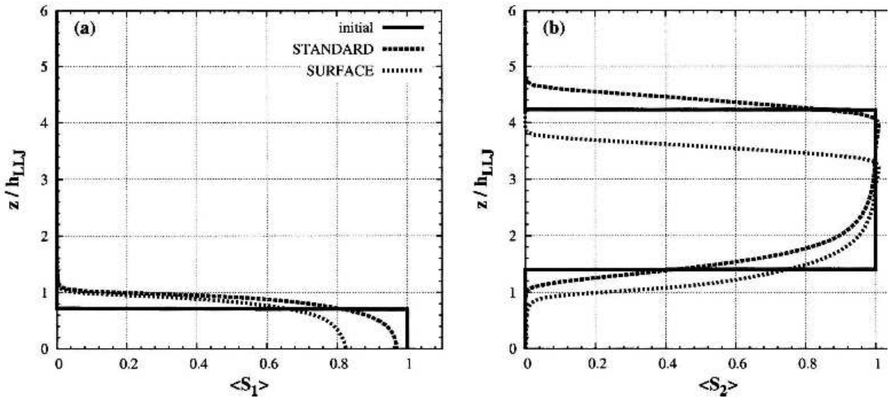

FIG. 8. Averaged scalar concentrations of (a) S_1 and (b) S_2 after 1 h (solid lines) and after 4 h (dotted lines from the beginning of the run. The y axis is normalized by the LLJ height (h_{LLJ}) obtained for each case.

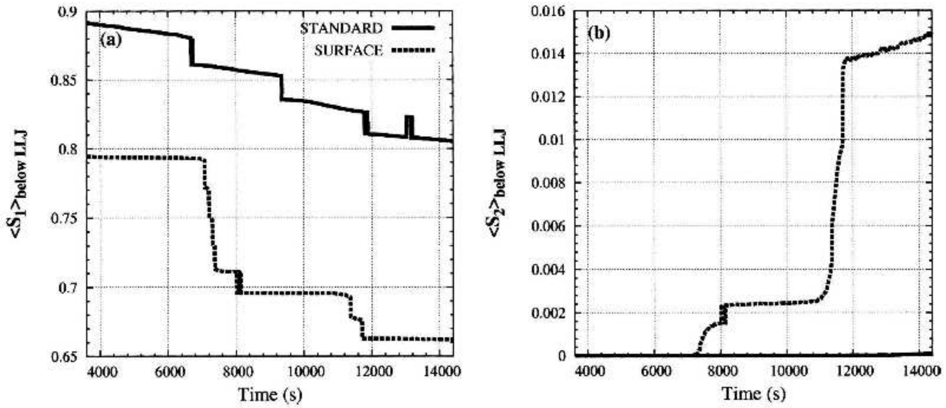

FIG. 9. Time series of the averaged scalar from the ground up to the LLJ height (h_{LLJ}): (a) S_1 and (b) S_2.

Baroclinity

$$\frac{\partial V_g}{\partial z} = \frac{g}{fT}\vec{k}X\nabla_h T \Rightarrow V_{g2} - V_{g1} = \int_{z1}^{z2}\left(\frac{g}{fT}\vec{k}X\nabla_h T\right)\delta z$$

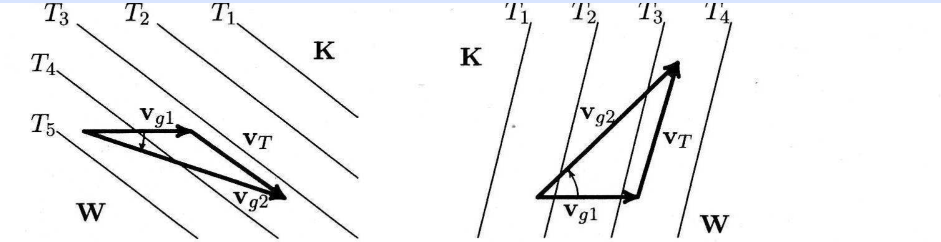

Bild 10.5 Zur Höhenabhängigkeit der geostrophischen Windrichtung. Es gelte $\mathbf{v}_{g1} = \mathbf{v}_g(z_1)$ und $\mathbf{v}_{g2} = \mathbf{v}_g(z_2)$ mit $z_1 < z_2$. Im linken Bildteil ist eine Warmluftadvektion dargestellt, die zu einer Rechtsdrehung des geostrophischen Windes mit der Höhe führt. Bei Kaltluftadvektion (rechtes Bild) dreht $\mathbf{v}_g$ dagegen nach links.

Warm advection: turns vg to right with height
Cold advection: to the left

Terrain-induced baroclinity =>

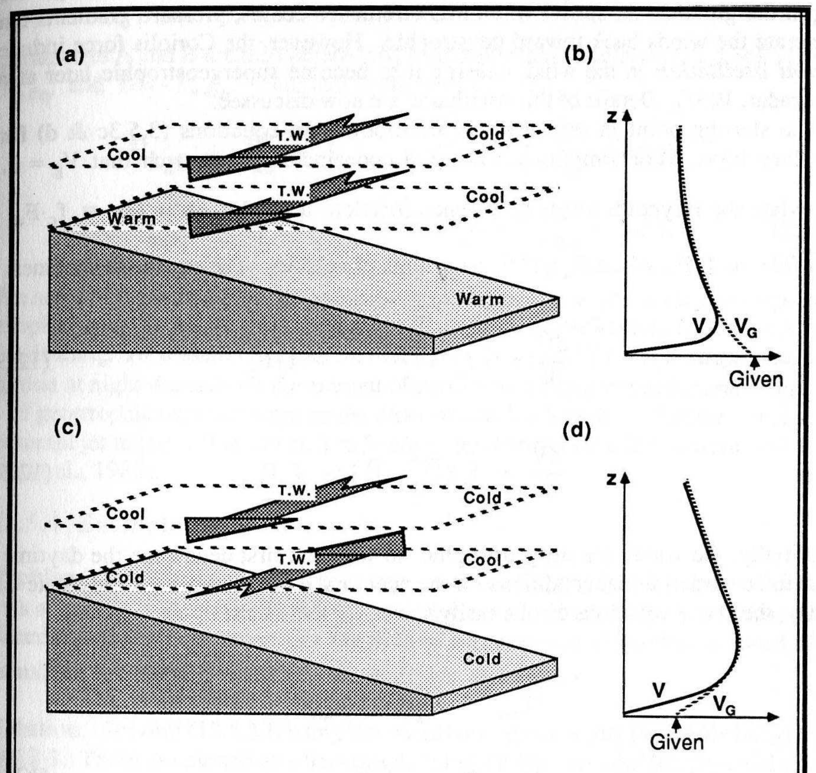

Fig. 12.17 Diurnal oscillation of the low level jet due to thermal wind (T.W.) forcings over sloping terrain.

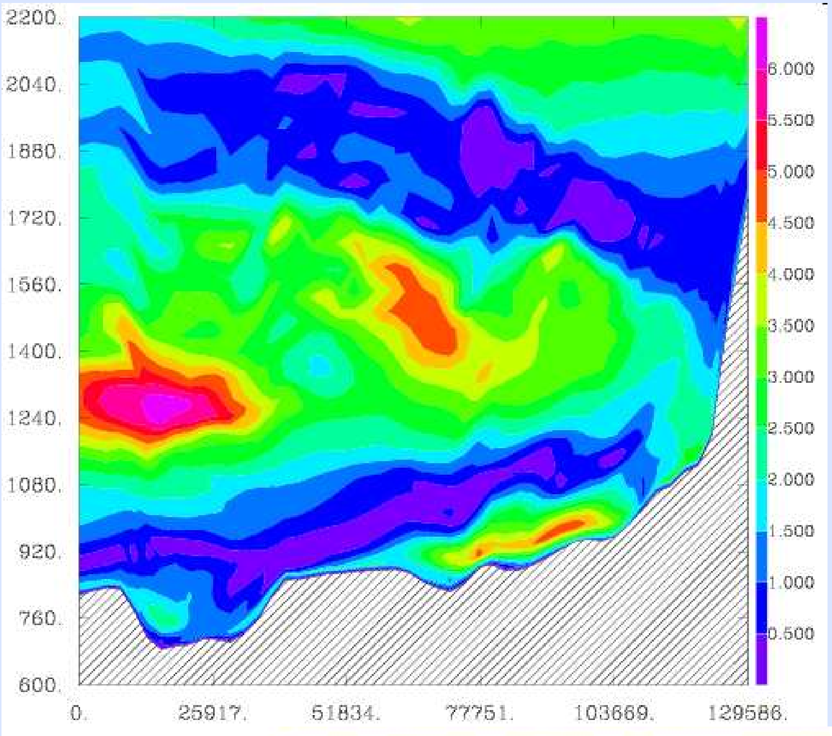

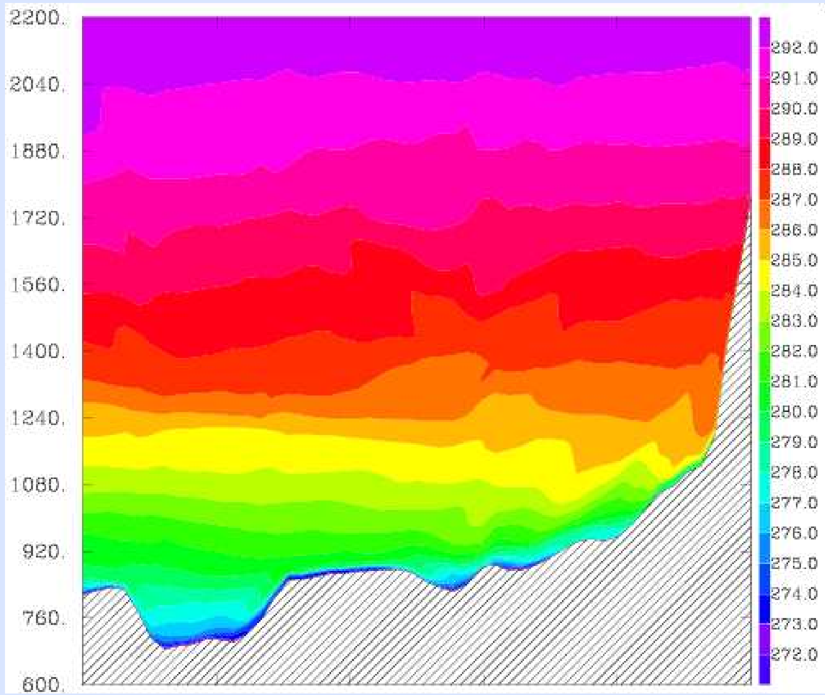

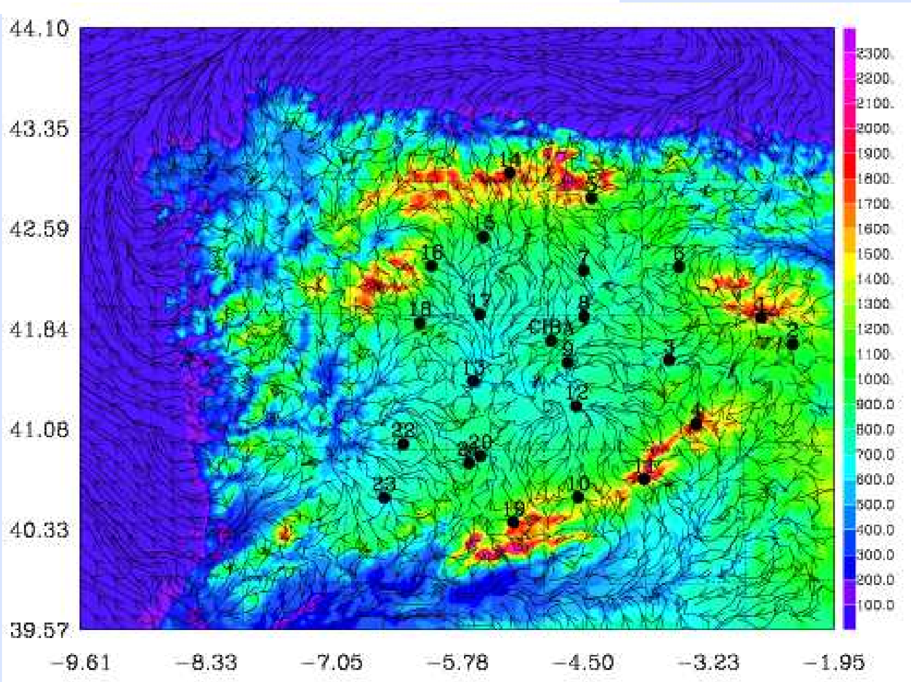

Katabatic flow

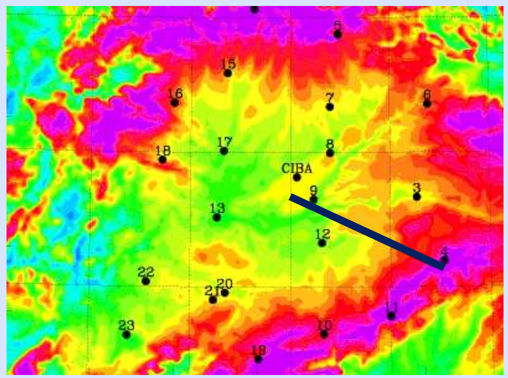

(Martinez/Cuxart 09)

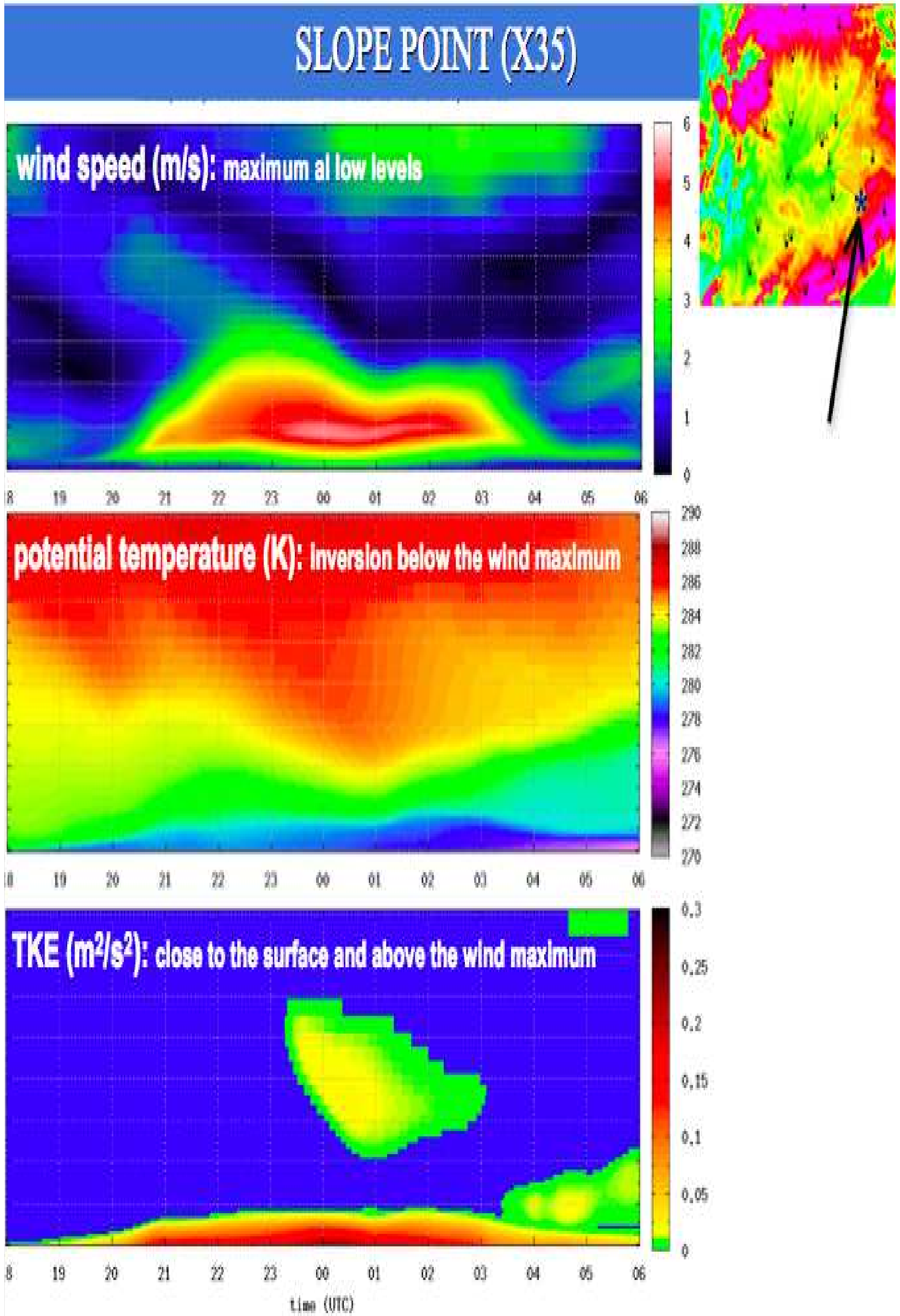
SLOPE POINT (X35)
wind speed (m/s): maximum al low levels
potential temperature (K): inversion below the wind maximum
TKE (m²/s²): close to the surface and above the wind maximum
time (UTC)

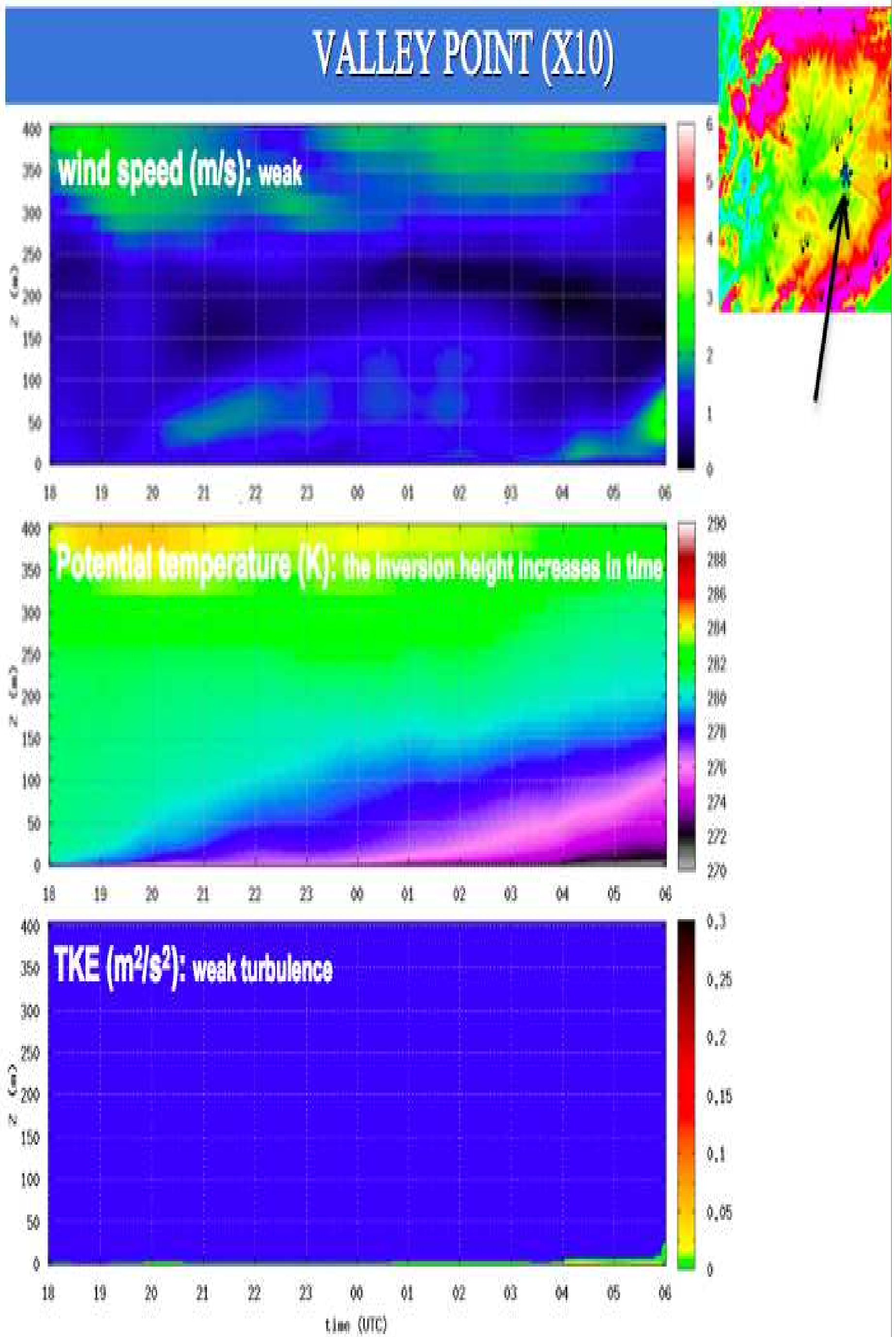
VALLEY POINT (X10)
wind speed (m/s): weak
Potential temperature (K): the inversion height increases in time
TKE (m²/s²): weak turbulence
z (m)
time (UTC)

$$U_{\mathrm{stor}} + U_{\mathrm{adv}} = U_{\mathrm{therm}} + U_b + U_{\mathrm{cor}} + U_{\mathrm{turb}} ,$$

$$T_{\mathrm{stor}} + T_{\mathrm{adv}} = T_{\mathrm{backadv}} + T_{\mathrm{rad}} + T_{\mathrm{turb}} .$$

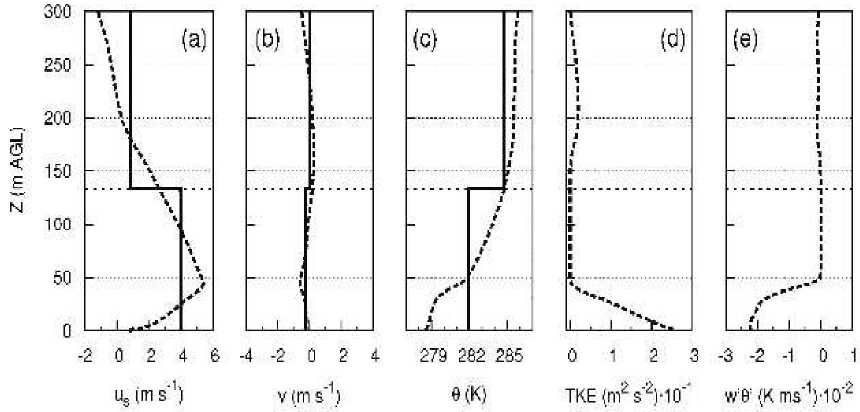

Fig. 6. Vertical profiles for: (a) along slope velocity (in m s^{-1}), (b) cross slope velocity (in m s^{-1}), (c) potential temperature (in K), (d) TKE (in m^2 s^{-2}), and (e) kinematic flux of latent heat (in K m s^{-1}) for the output of the mesoscale model (dashed line) and the result after applying the hydraulic approach (bold line) for point *u* (Fig. 5) at 00:00 UTC.

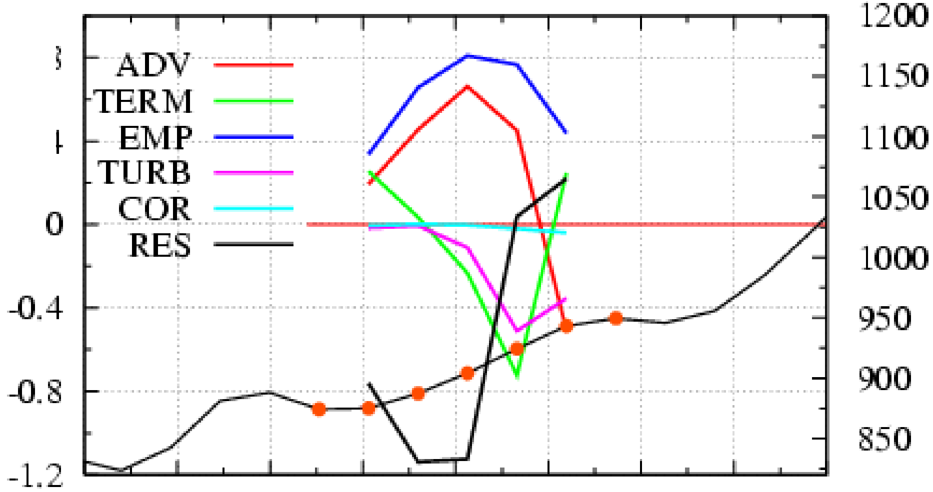

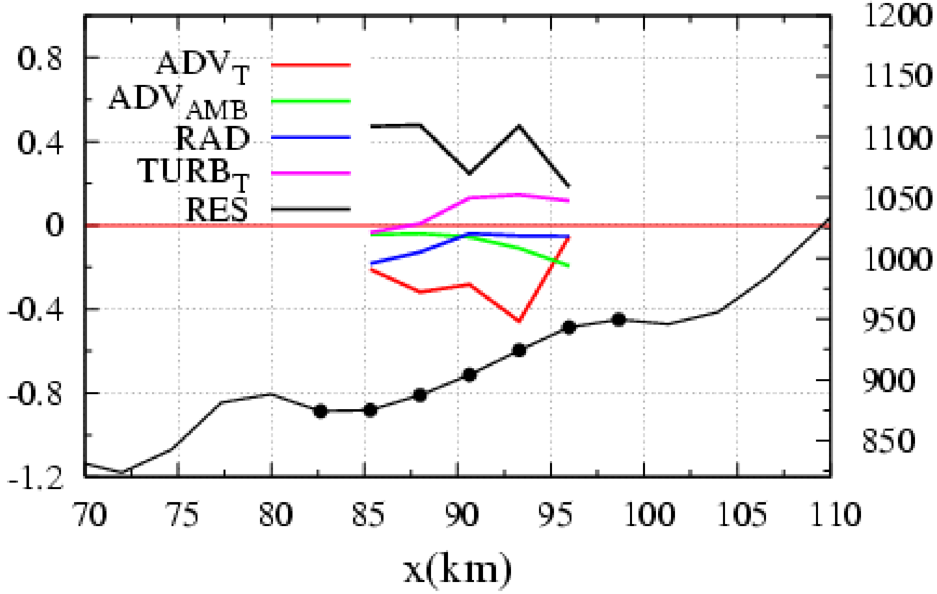

(Martinez/Cuxart 09)

Valley-Plain winds

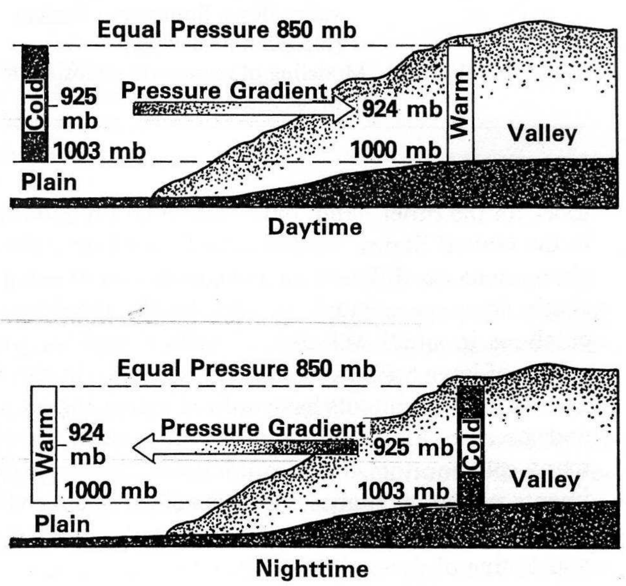

FIG. 2.2. Illustration of the thermal forcing of valley-plain pressure gradients leading to the development of an along-valley wind system. (Adapted from Hawkes 1947.)

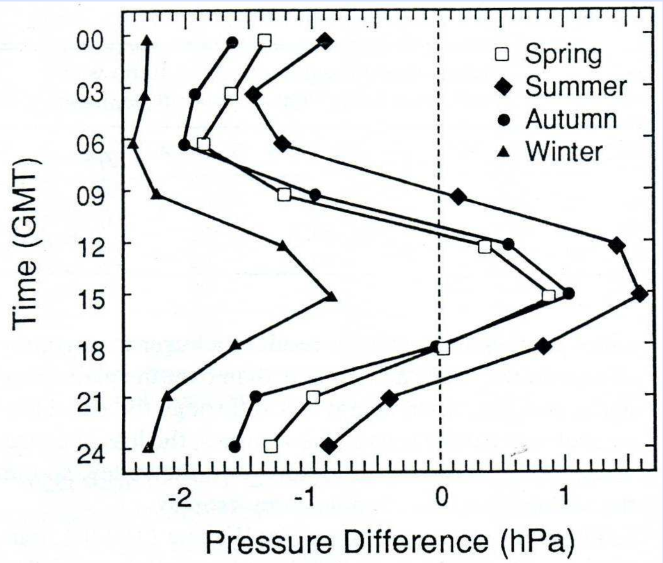

FIG. 2.3. Daily march of horizontal pressure gradient at 550 m MSL between a plain station (Munich) and a deep valley station (Innsbruck), sunny days. (Nickus and Vergeiner 1984.)

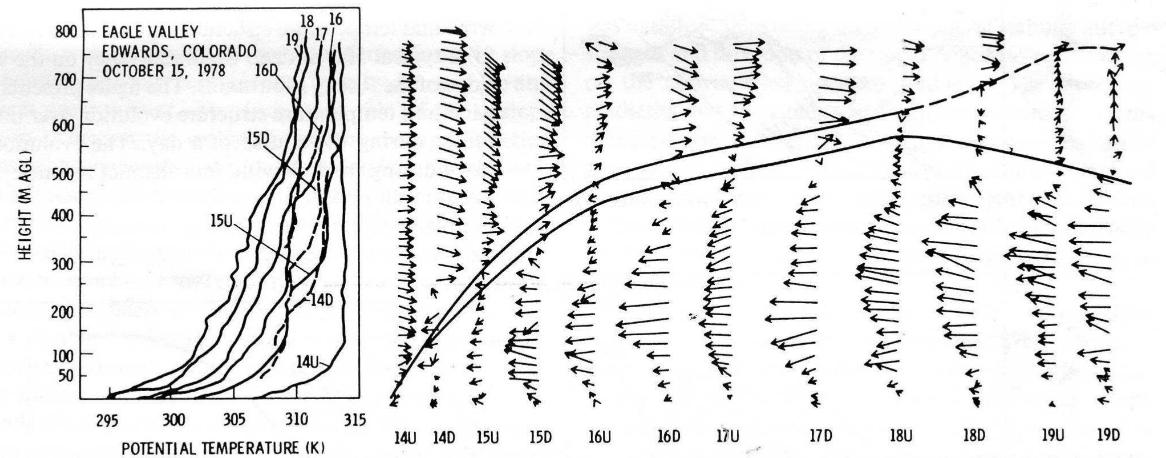

#	TIME (MDT)	#	TIME (MDT)	#	TIME (MDT)
14U	1802-1820	16U	1931-1947	18U	2100-2118
14D	1820-1836	16D	1947-2001	18D	2118-2133
15U	1846-1903	17U	2014-2031	19U	2143-2202
15D	1903-1922	17D	2031-2045	19D	2202-2216

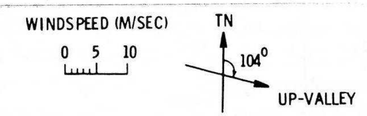

FIG. 2.28. Temperature and wind structure evolution during the evening transition in the 700-m-deep Eagle Valley on 15 October 1978, ustrating the rapid development of the down-valley wind system and the growth of the temperature inversion. Note that small-scale features in e temperature structure are maintained from sounding to sounding. In the figure, vector winds are plotted as a function of height; vector lengths rrespond to wind speeds (see wind speed legend). The up-valley direction is given for reference. The time intervals over which the up (U) and own (D) soundings were conducted are given in the table. The solid lines in the wind profiles delineate the boundaries of the wind transition ver. (Whiteman 1986.)

(Whiteman 1990)

Basin Heterogeneity

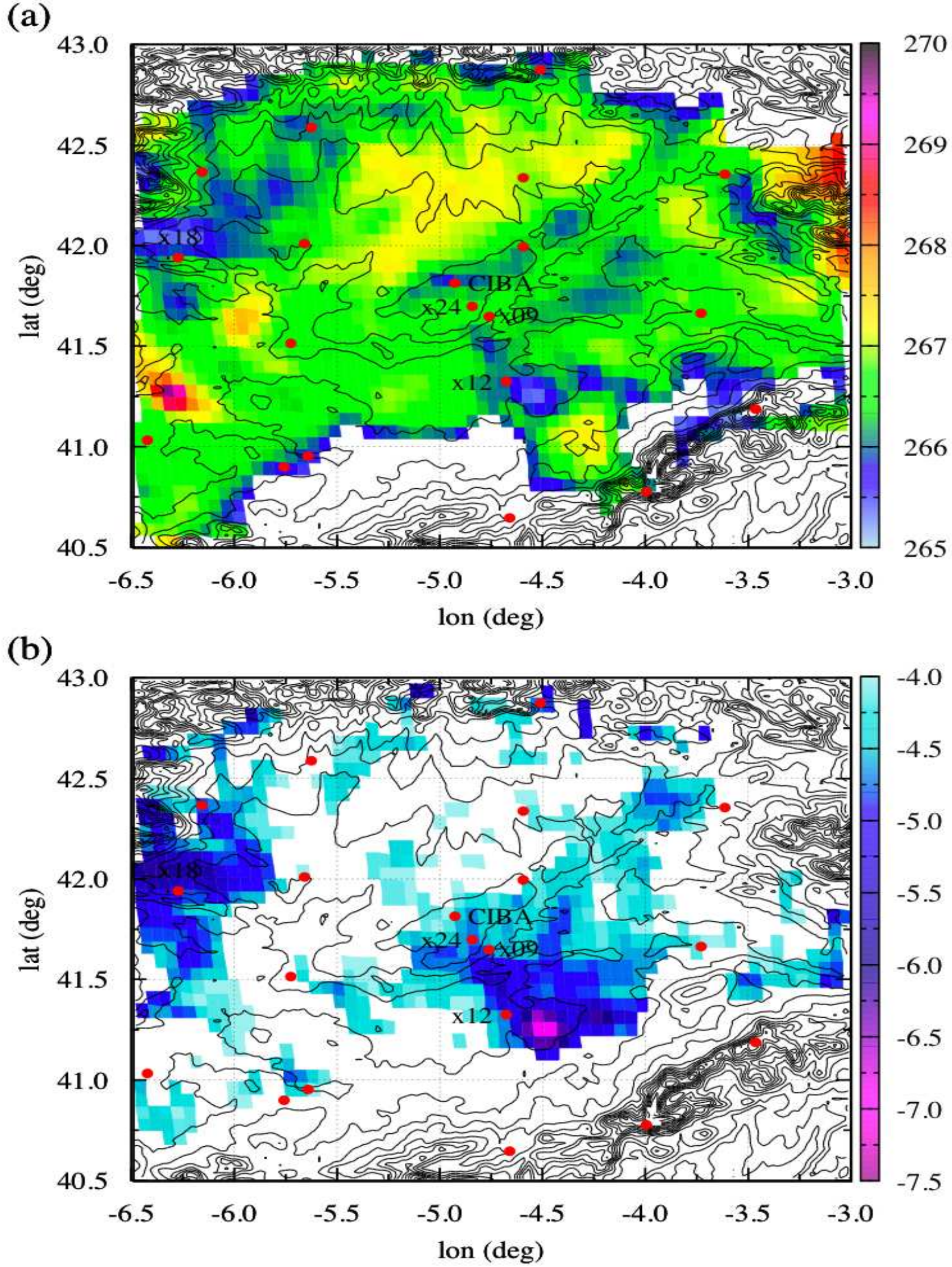

Fig. 4 (a) Mean nocturnal temperature $\overline{T}_b(\mathbf{x})$ for the Duero basin derived from Meteosat-7 (without the snow area). (b) Total cooling from the beginning of the night (1730 UTC) to just before sunrise (0730 UTC). Only points with a total cooling equal or higher than 4 K are represented. In both plots, surface elevation contours are plotted every 100 m within the range 500 - 2100 m ASL. The locations of the AWS from AEMET are displayed with dots.

(Martinez et al 10)

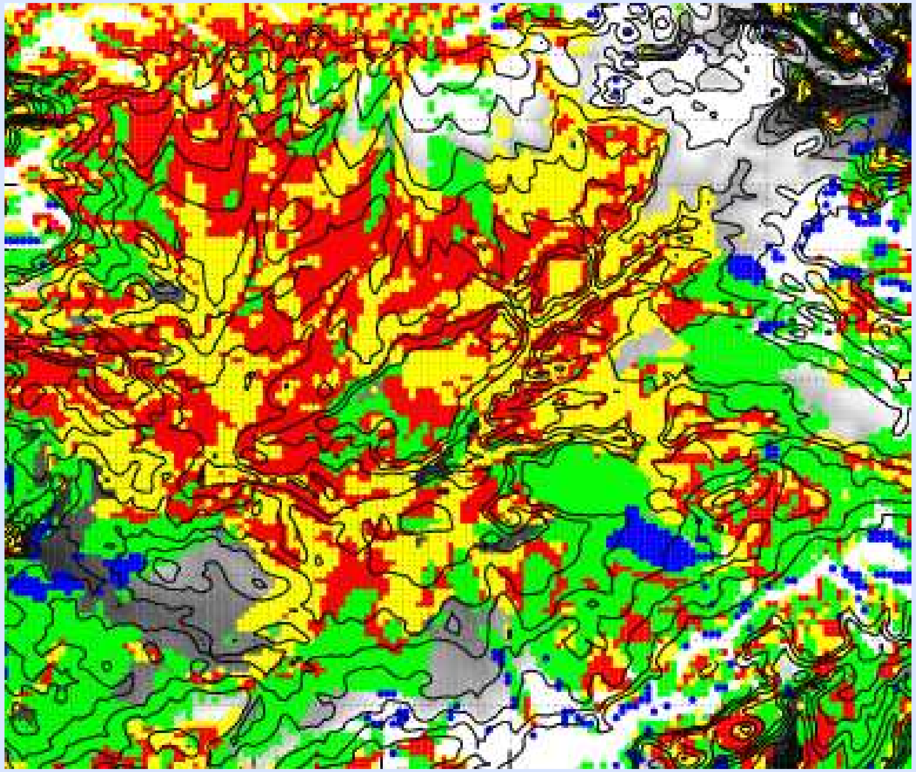

weak/moderate/strong/no jet

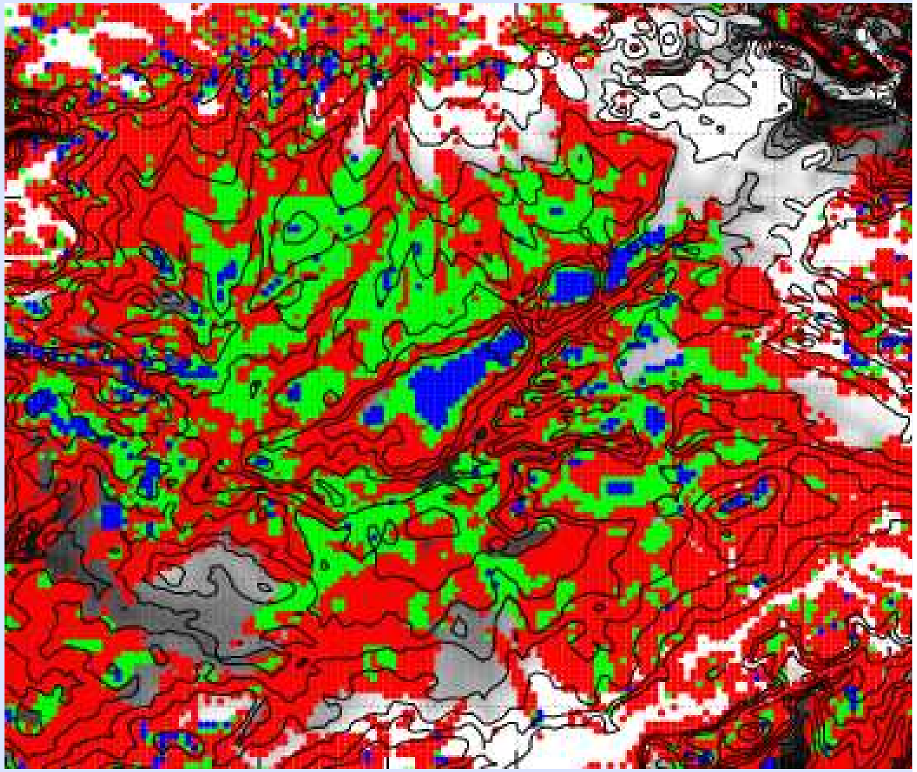

Weak/moderate/Strong st.

Table 1 Percentage of the cases (19430 in total) for the classification of the points at 0000 UTC according to the wind maxima (up to 100 m) and the temperature gradient (up to 10 m where $\Delta\theta = \theta_{10.5m} - \theta_{1.5m}$). The jet category is counted when the wind above the jet is, at least, 0.5 m s^{-1} smaller than in the jet height.

	$\Delta\theta < 0$ K	$0 \leq \Delta\theta < 2$ K	$2 \leq \Delta\theta < 4$ K	$\Delta\theta \geq 4$ K	Total
weak jet ($0.5 \leq wind_{max} < 2$ m s^{-1})	0.04	18.08	6.85	1.02	**25.99**
moderate jet ($2 \leq wind_{max} < 4$ m s^{-1})	0.02	21.98	2.17	0.25	**24.42**
strong jet ($wind_{max} > 4$ m s^{-1})	0.00	2.30	0.07	0.00	**2.37**
no jet-weak ($wind_{below100m} < 2$ m s^{-1})	0.08	12.10	8.32	2.05	**22.55**
no jet-moderate ($wind_{below100m} \geq 2$ m s^{-1})	0.12	20.45	3.29	0.81	**24.67**
total	**0.26**	**74.91**	**20.70**	**4.13**	**100.00**

(Martinez et al 10)

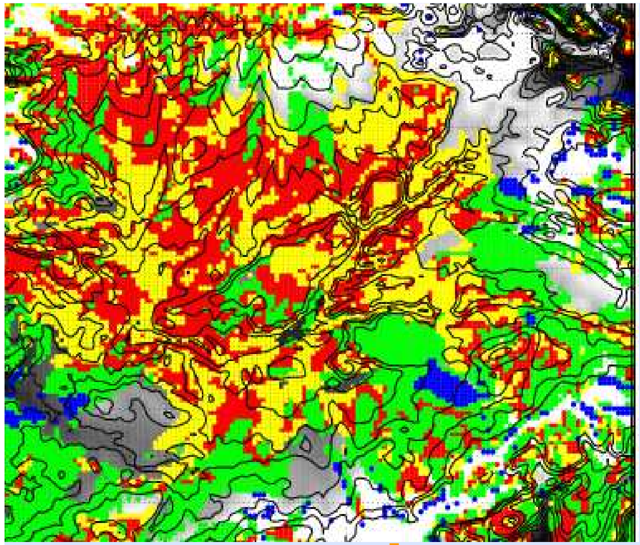

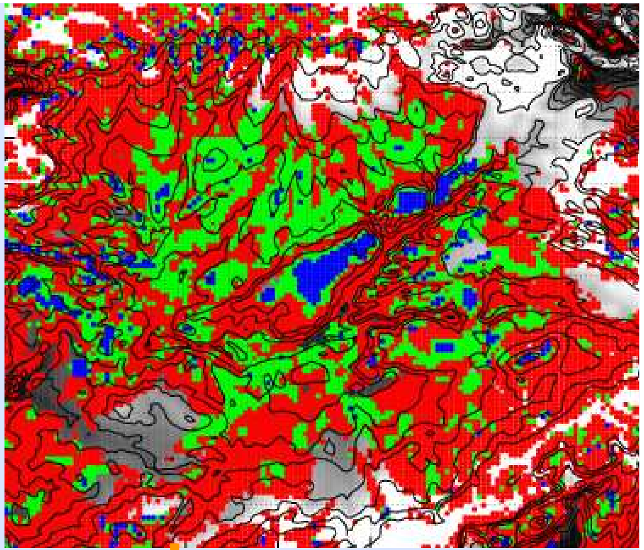

averaged profiles for each classified category

(Martinez et al 10)

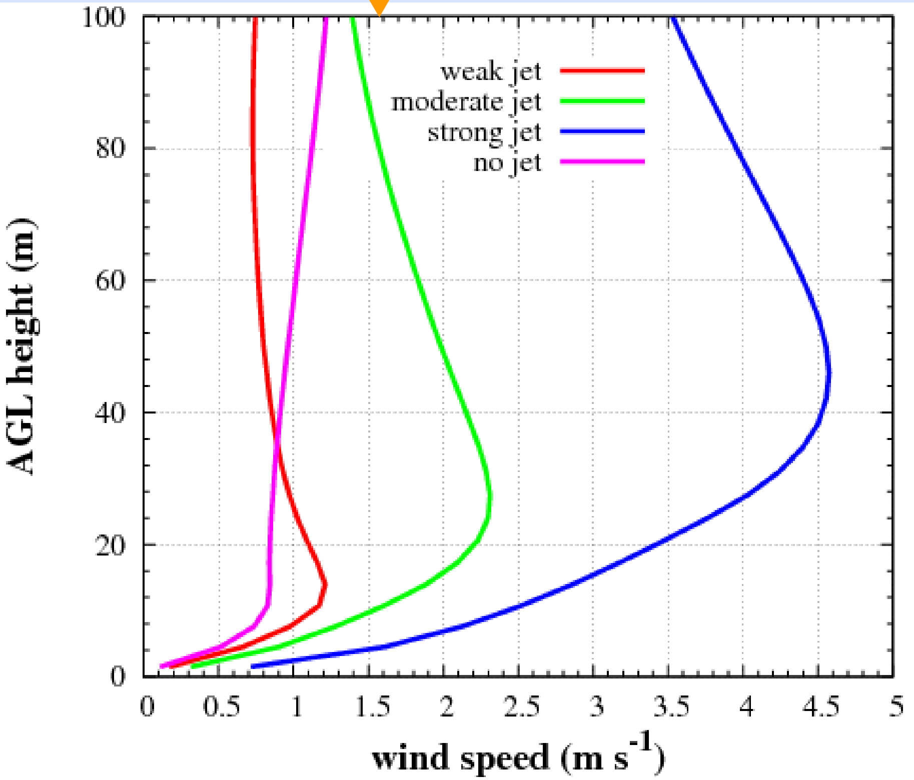

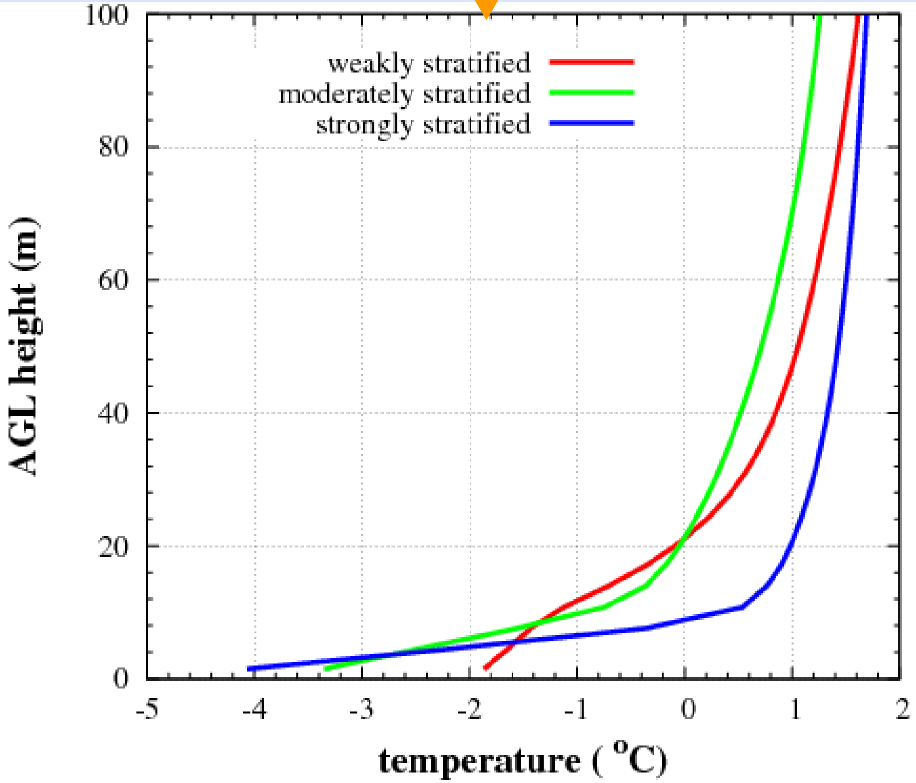

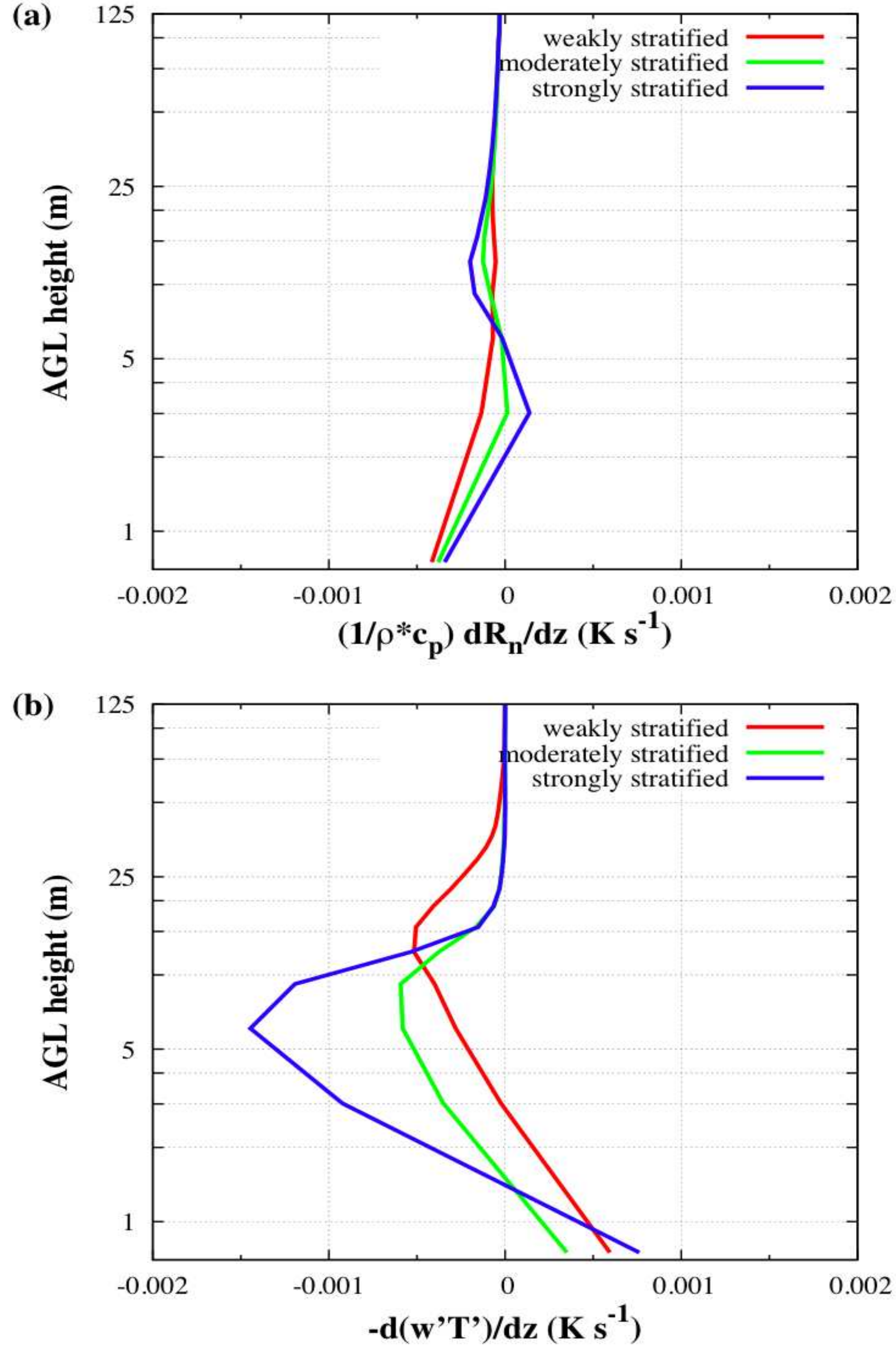
(a)
weakly stratified
moderately stratified
strongly stratified
AGL height (m)
125
25
5
1
-0.002
-0.001
0
0.001
0.002
$(1/\rho*c_p)\ dR_n/dz\ (K\ s^{-1})$
(b)
weakly stratified
moderately stratified
strongly stratified
AGL height (m)
125
25
5
1
-0.002
-0.001
0
0.001
0.002
-d(w'T')/dz $(K\ s^{-1})$

Extremely weak turbulence: submeso motions

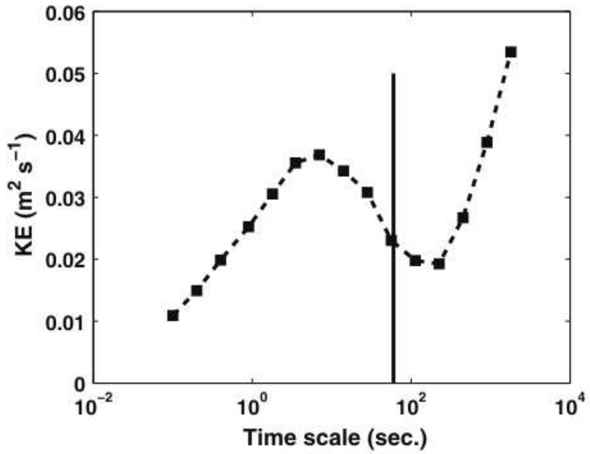

Fig. 1 The scale dependence of the horizontal kinetic energy for the entire turbulence and submeso range of time scales composited over all of the nocturnal records for the Iowa network. The vertical line designates the 1-min time scale used to pragmatically separate turbulence and submeso motions for all of the networks. This study concentrates on submeso scales to the right of the vertical line

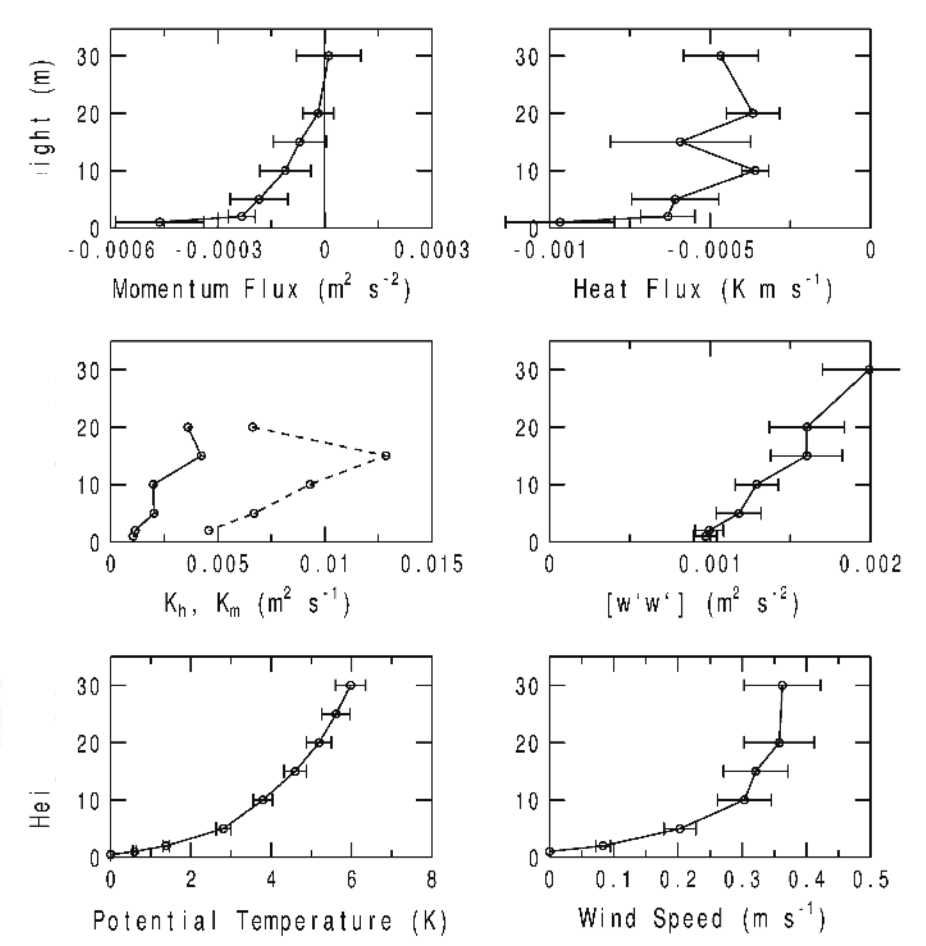

Mahrt (2008)

Mahrt and Vickers (2006)

Closure of the surface energy budget

Radiation + Soil Flux = Turbulence exchange (heat and moisture)
$R_{n0} + G_0 = H_0 + \lambda E_0$
It should close, it does not!
From Foken (2008): imbalances above 30% over bare soil, short grass, agricultural land, down to 10% over more homogeneous surfaces like irrigated cotton fields or wheat fields.
For a particular experiment over grass, Foken attributes the errors mainly to measuring processes

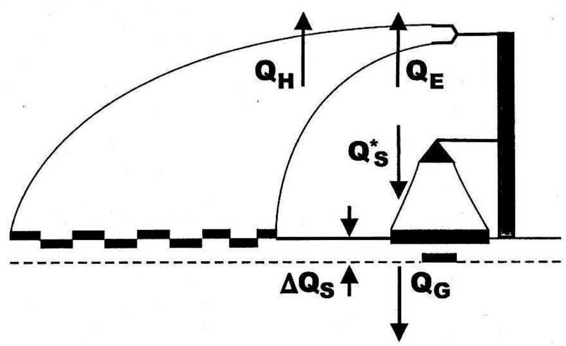

Fig. 3.34. Schematic view of the measuring area of the different terms of the energy balance equation

Latent: 5 to 20%
Sensible: 10 to 20%
Net radiation: 10 to 20%
Ground: up to 50%
Storage and others: unknown

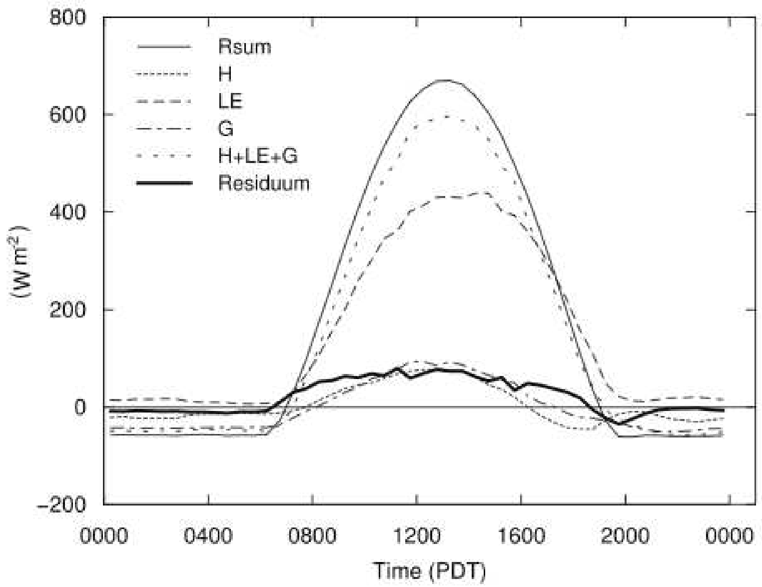

Fig. 6 The diurnal composite of the surface energy balance for EBEX from all sites over the entire measurement period. Shown are the "Major Terms" described in Sect. 5

Oncley et al (2007)

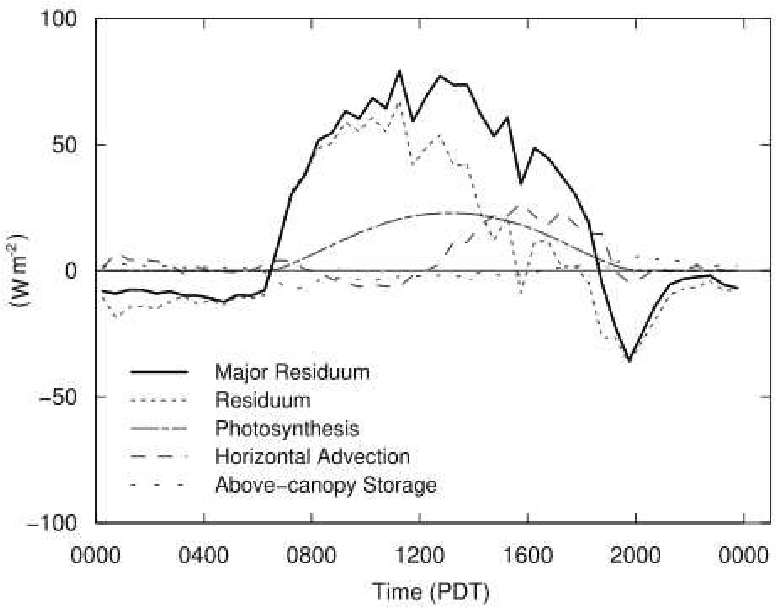

Fig. 9 The diurnal composite of the minor surface energy balance terms, along with the residuum found from the major terms for EBEX from all sites over the entire measurement period

Radiation (no wind)

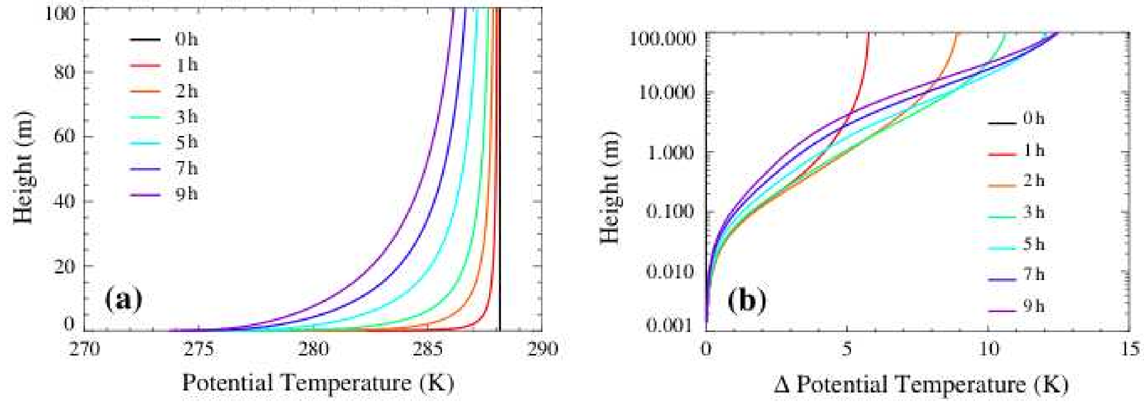

Fig. 1 Profiles of potential temperature at hourly and subsequently two-hourly intervals. **a** With a linear height scale. **b** With a logarithmic height scale, showing the difference from the surface temperature

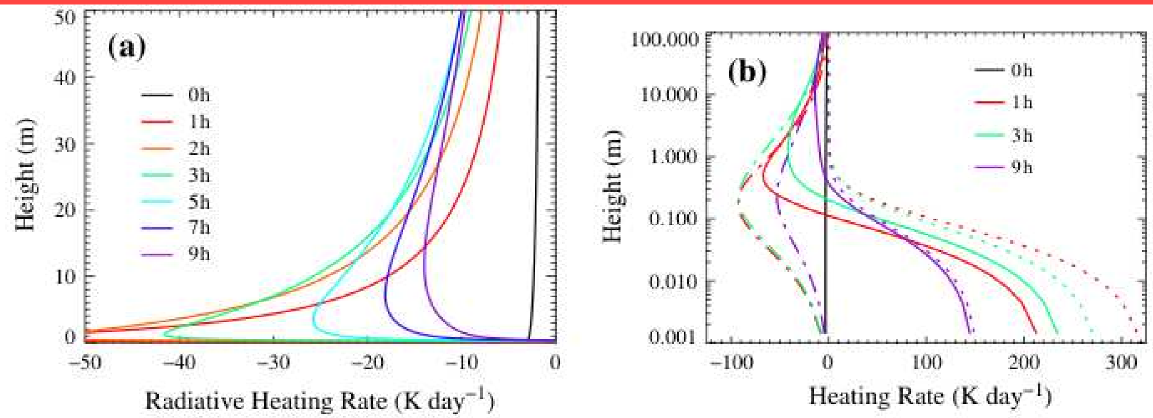

Fig. 2 Profiles of the radiative heating rates at hourly and subsequently two-hourly intervals. **a** Actual radiative heating rates on a linear height scale. **b** On a logarithmic height scale, showing actual radiative heating rates (solid), *minus* the conductive heating rates (dotted) and the portion of the radiative cooling rate due to direct cooling to the surface (dot-dashed)

Edwards (2009)

Dew

Saturation can occur
near the surface

Condensation implies
release of heat to environment

Up to 1 l/m^2 in one night

SEB modified

In a small closed valley in the Alps, Whiteman et al (2006) estimated that the dew reduces to 1/3 to 1/2 half the nocturnal cooling

Garratt (1992)

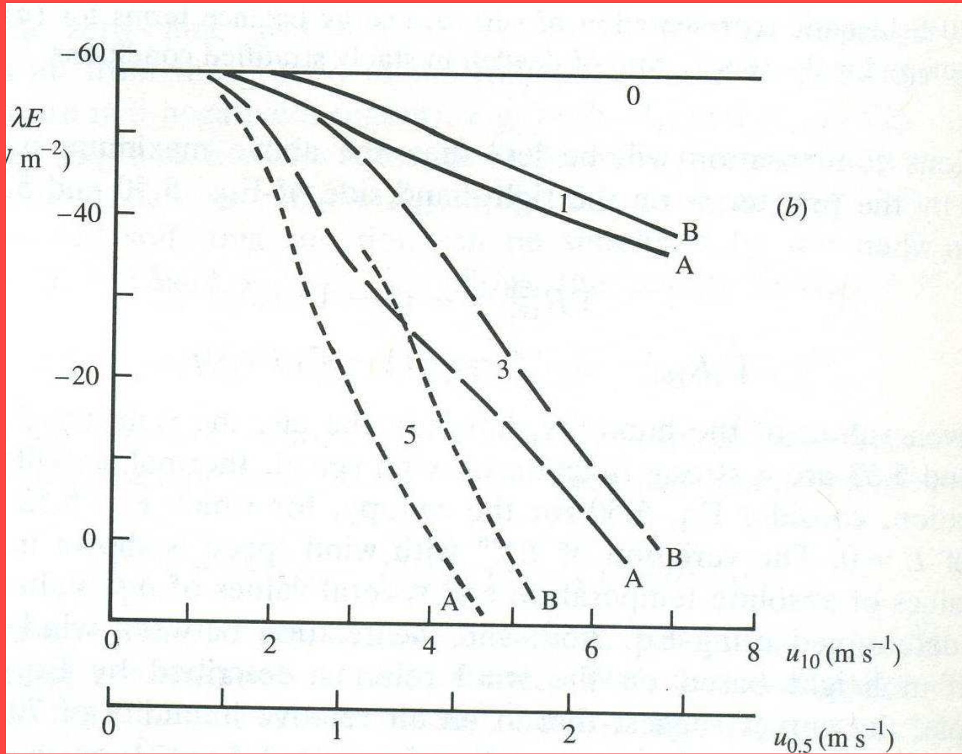

T=293K, A:ΔT=0.6K, B: ΔT=2.5K

100%, 79%, 66%

Fog

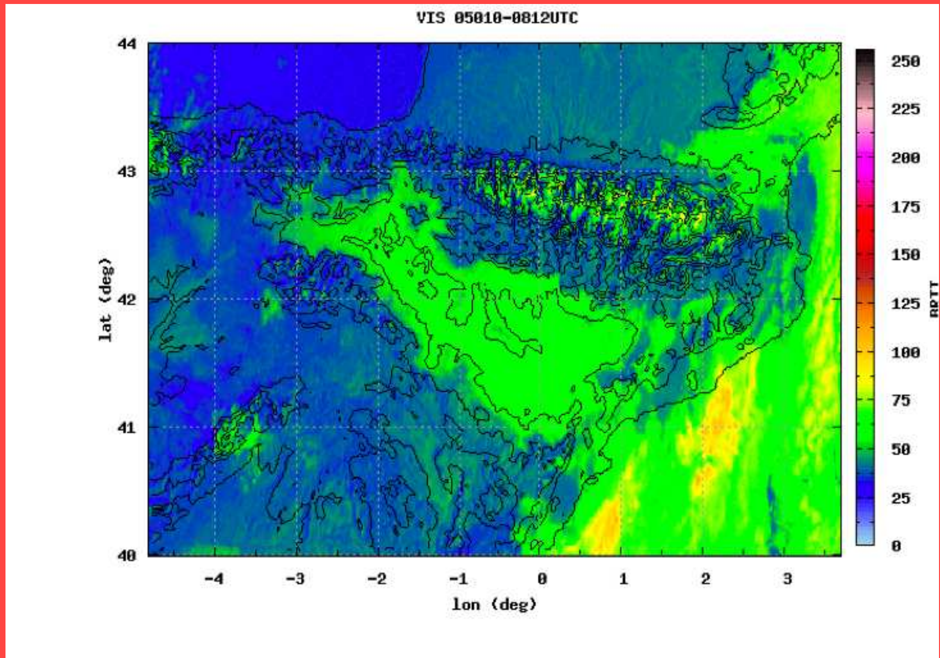

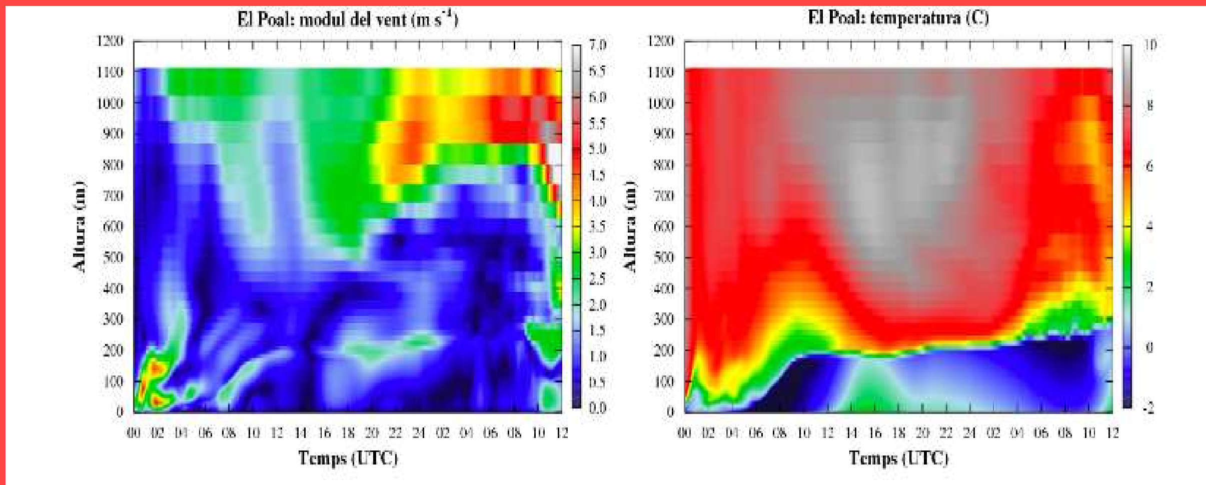

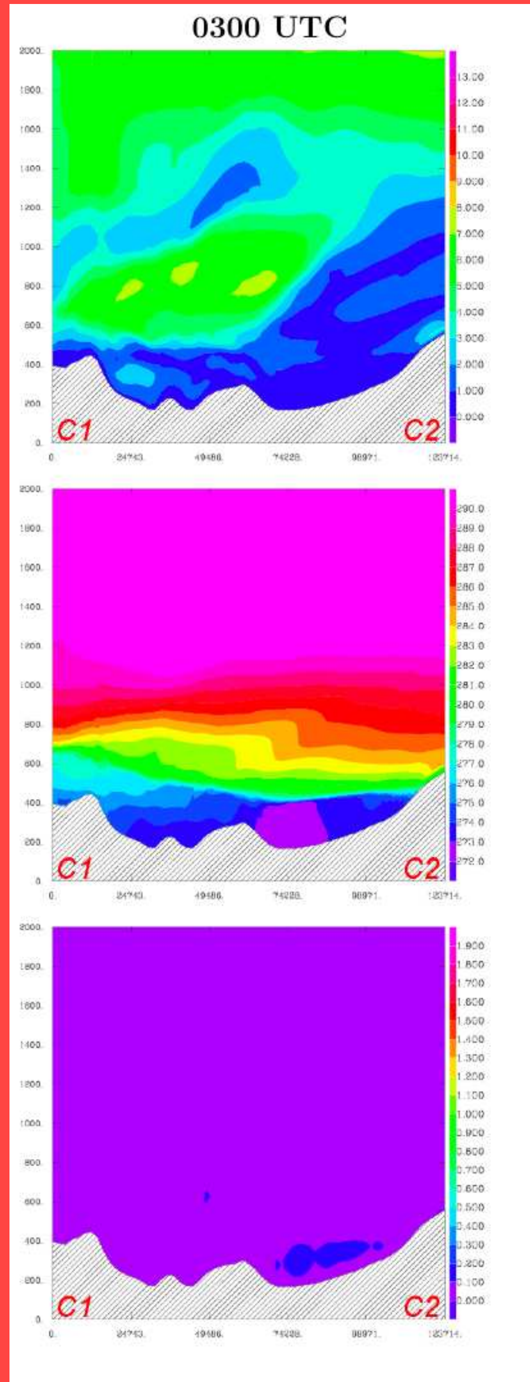

(Cuxart et al 10)

Summary

Nocturnal turbulence needs wind (except for compact fog)

Circulations develop when pressure gradient exist (all scales)

LLJ seem to be everywhere and generate turbulence, either continuous or sporadic

Runaway cooling may not be happening because of radiation, condensation and small scale motions near the ground

Open: waves, surface layer, anisotropic turbulence theory (?), interaction with other processes (phase changes, radiation), surface heterogeneity (including topography)

Temperature curvature

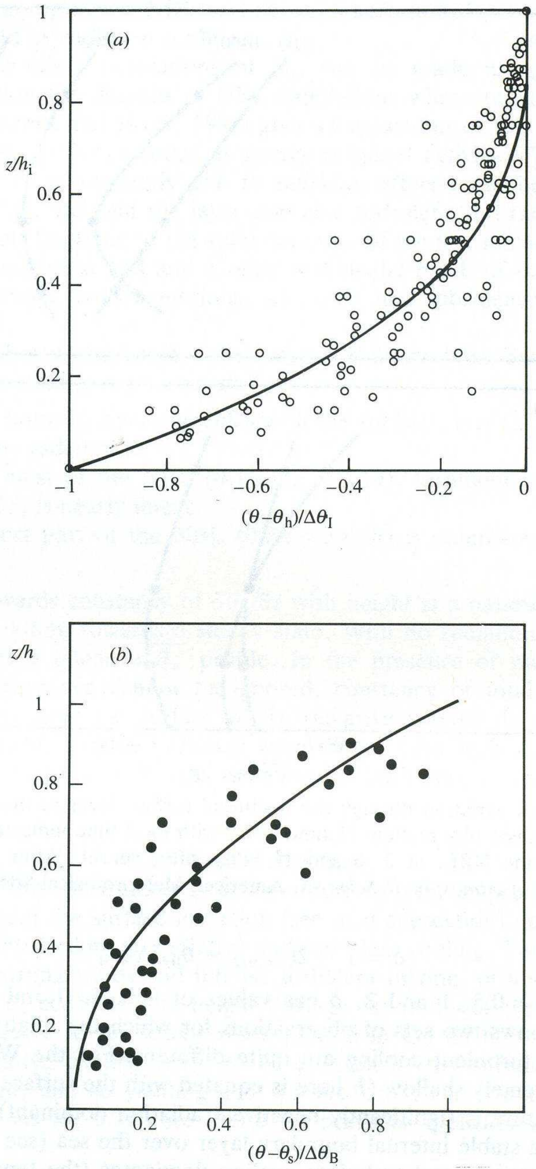

Fig. 6.17 (*a*) Normalized θ profiles for the night-time WANGARA data, where h_i is the surface inversion height. The solid curve represents Eq. 6.72 with $m = 3$. After Yamada (1979), *Journal of Applied Meteorology*, American Meteorological Society. (*b*) Normalized θ profiles for a stably stratified internal boundary layer (of depth h) over the sea; the sea-surface temperature is denoted by θ_s. The solid curve represents Eq. 6.71 with $n = 2$. From Garratt and Ryan (1989): reprinted by permission of Kluwer Academic Publishers.

Radiation dominates
Negative curvature (convex)

Turbulence prevails
Positive curvature (concave)

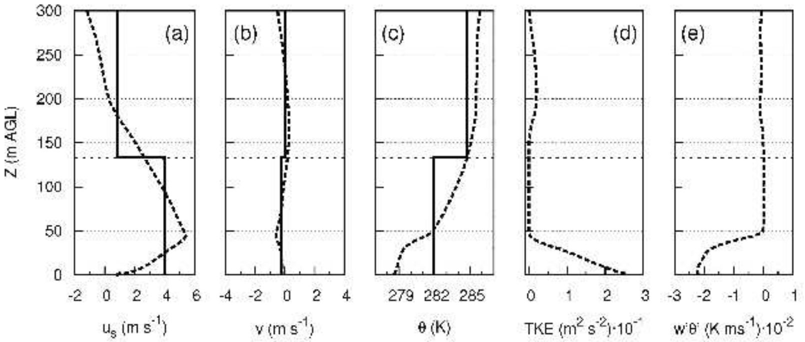

Fig. 6. Vertical profiles for: (a) along slope velocity (in m s^{-1}), (b) cross slope velocity (in m s^{-1}), (c) potential temperature (in K), (d) TKE (in m^2 s^{-2}), and (e) kinematic flux of latent heat (in K m s^{-1}) for the output of the mesoscale model (dashed line) and the result after applying the hydraulic approach (bold line) for point *u* (Fig. 5) at 00:00 UTC.

$$\frac{\partial}{\partial t}\left(\overline{\overline{u_s}}\right) + \overline{\overline{u_s}}\frac{\partial}{\partial s}\left(\overline{\overline{u_s}}\right) + \overline{\overline{w_n}}\left(\frac{u_h-\overline{\overline{u_s}}}{h}\right)$$
$$= -\frac{g}{\theta_0}\frac{\partial}{\partial s}\left(h\overline{\overline{\Delta\theta}}\right)\cos\alpha + g\frac{\overline{\overline{\Delta\theta}}}{\theta_0}\sin\alpha + f\overline{\overline{v}} - \frac{\left(\overline{w_n'u_s'}\right)_h - \left(\overline{w_n'u_s'}\right)_0}{h},$$

$$\frac{\partial}{\partial t}\left(\overline{\overline{\Delta\theta}}\right) + \overline{\overline{u_s}}\frac{\partial}{\partial s}\left(\overline{\overline{\Delta\theta}}\right) + \overline{\overline{w_n}}\left(\frac{\Delta\theta_h-\overline{\overline{\Delta\theta}}}{h}\right)$$
$$= \gamma\left(\overline{\overline{w_n}}\cos\alpha - \overline{\overline{u_s}}\sin\alpha\right) + \frac{1}{\rho_0 C_p}\frac{R_h-R_0}{h} + \frac{\left(\overline{w_n'\theta'}\right)_h - \left(\overline{w_n'\theta'}\right)_0}{h}$$

$$\frac{\partial}{\partial s}\left(\overline{\overline{u_s}}\right) + \left(\frac{w_h-\overline{\overline{w_n}}}{h}\right) = 0,$$

$$U_{\mathrm{stor}} + U_{\mathrm{adv}} = U_{\mathrm{therm}} + U_b + U_{\mathrm{cor}} + U_{\mathrm{turb}},$$

$$T_{\mathrm{stor}} + T_{\mathrm{adv}} = T_{\mathrm{backadv}} + T_{\mathrm{rad}} + T_{\mathrm{turb}}.$$

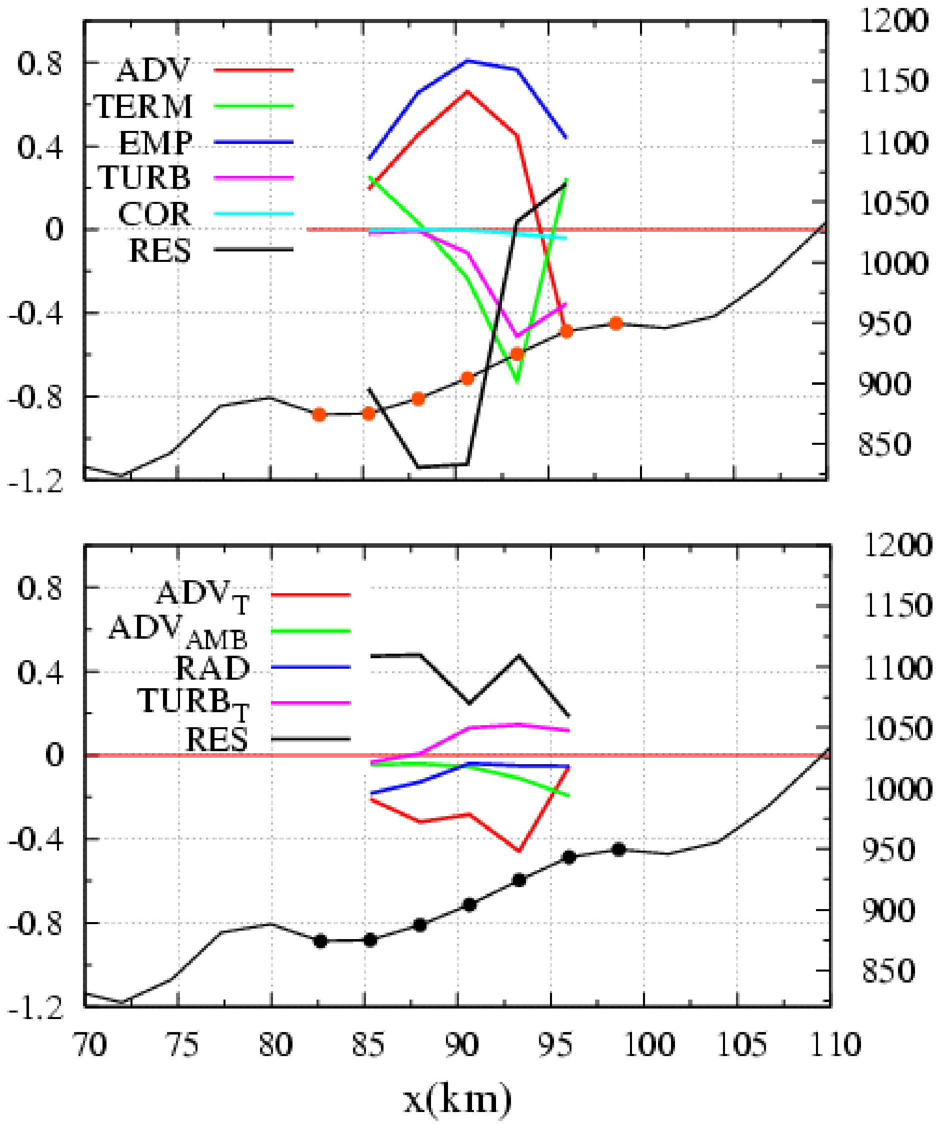

Comparison with observations (SABLES 98)

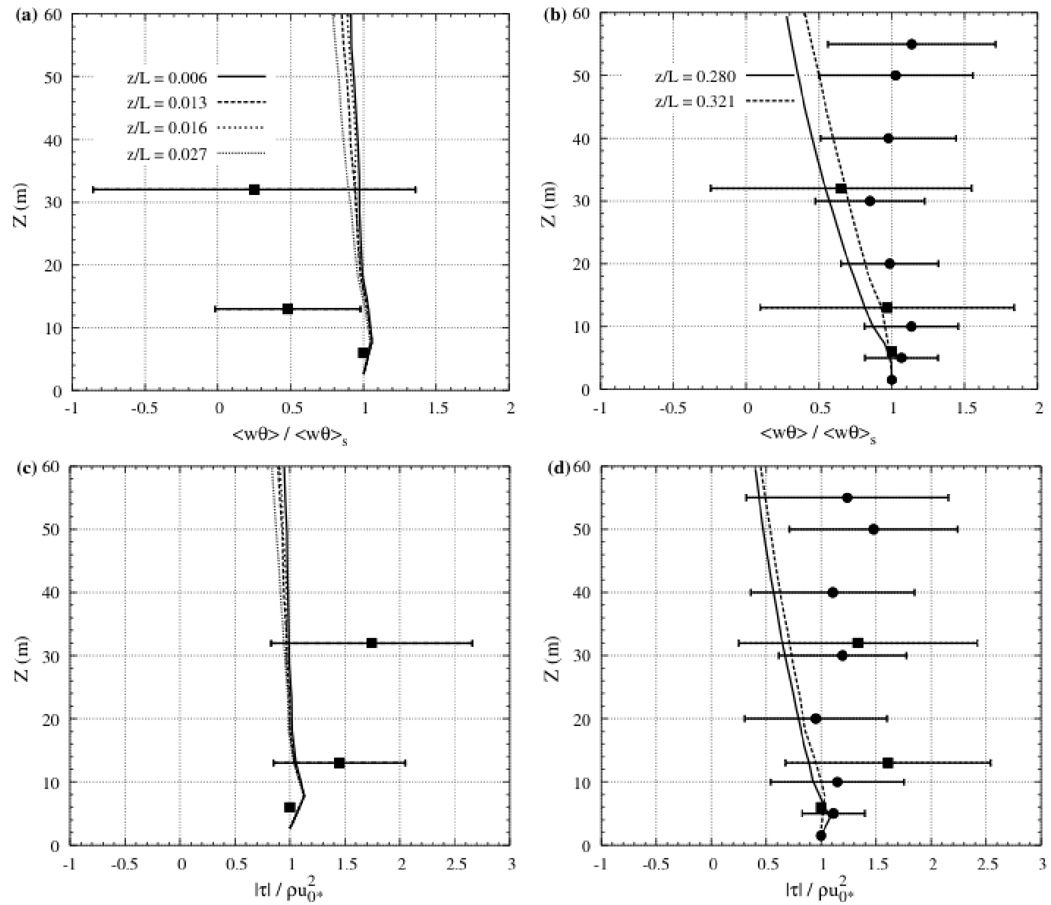

Figure 8. Comparison to observations: normalized vertical kinematic heat flux and Reynolds shear stress for $0 < z/L \leq 0.03$ ((a) and (c)) and $0.25 < z/L \leq 0.40$ ((b) and (d)). Symbols as in Figure 7.

Fluxes do not decrease with height

*Air near the surface cools and becomes denser that environment air at the same level: primary forcing

* Downslope flows are established, maximum winds between 1 and 6 m/s at heights below 40 m depending on the scale of the slope.
* Motions can be pulsating as the flow relaxes the difference of temperatures
* Flow can be decoupled from the surface and from air above
* Long slope flows are also affected by basin baroclinity or even Coriolis force
* Turbulence may occur close to the ground or elevated: episodic mixing/ thermal belt
* Organized return circulations not obvious.

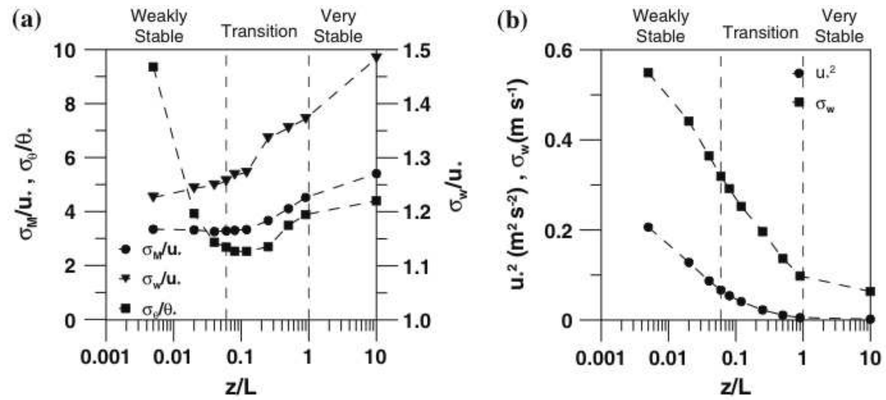

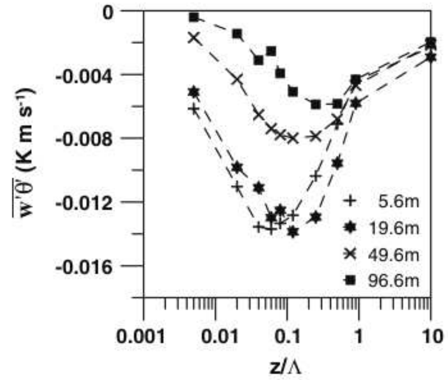

Fig. 3 Dependence on the local stability parameter z/Λ (logarithmic scale) for: (**a**) the standard deviation of the horizontal wind scaled with the local friction velocity, the standard deviation of the vertical velocity scaled with the local friction velocity and the standard deviation of the potential temperature scaled with the local temperature scale, and (**b**) the vertical flux of the horizontal momentum u_*^2 and the standard deviation of the vertical velocity (now, unscaled). All the values are at 5.6 m height. The dashed line marks the CIBA limits F1 and F2 between regimes

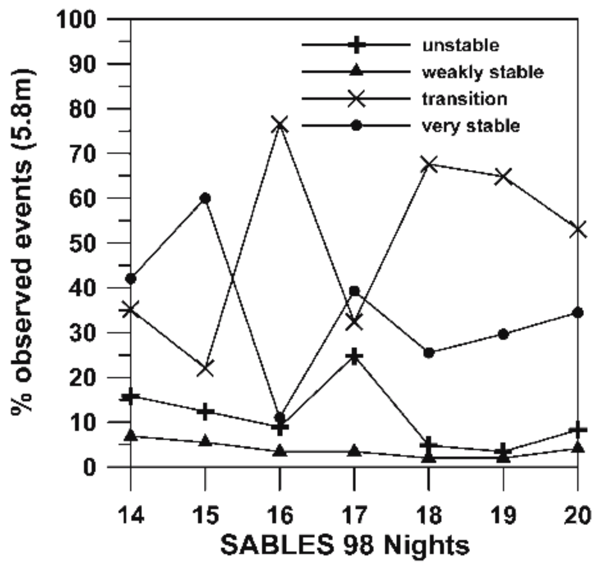

gure 2. Proportion of each stability type, for the period 14–20 September 1998 during the BLES 98 campaign, at a height of 5.8 m.

TABLE II

(a) Percentages at which the measurement of turbulence kinematic heat flux ($-\overline{w'\theta'}$) is larger for every recording height. (b) Same as (a) except for turbulence kinetic energy.

(a) Maximum wind at:	Maximum kinematic heat flux ($-\overline{w'\theta'}$) is at height of:			
	5.6 m	19.6 m	49.6 m	96.6 m
34.6 m	66.6	18.2	6.1	9.1
49.6 m	49.4	43.8	0.0	6.8
74.6 m	48.4	32.2	9.7	9.7
(b) Maximum wind at:	Maximum TKE is at height of:			
	5.6 m	19.6 m	49.6 m	96.6 m
34.6 m	33.3	21.2	18.2	27.3
49.6 m	21.3	38.2	9.0	31.5
74.6 m	38.7	9.7	12.9	38.7

30-min average data were used, from the 100-m CIBA tower during the period September 2002 to June 2003, when a wind maximum at 34.6 m, 49.6 m or 74.6 m was detected.

Averaged profiles over 1h

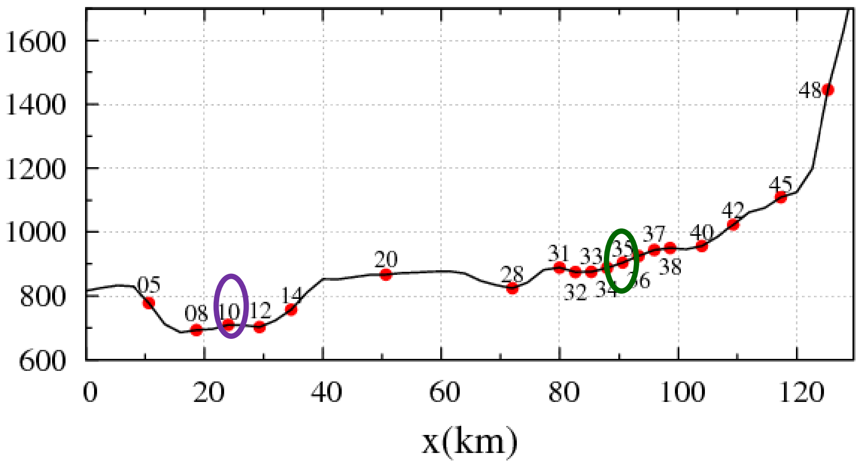

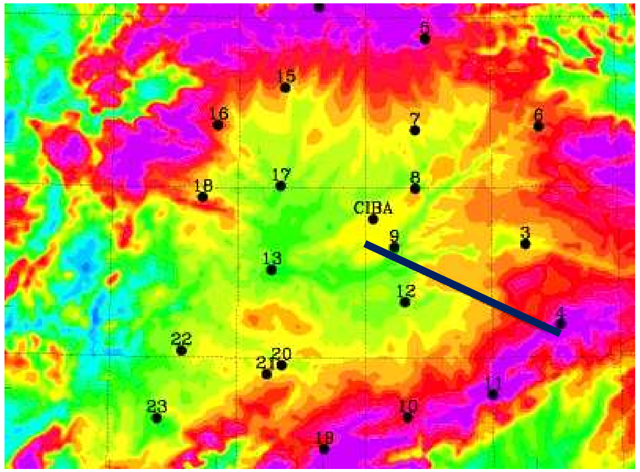

valley (X10)

slope (X35)

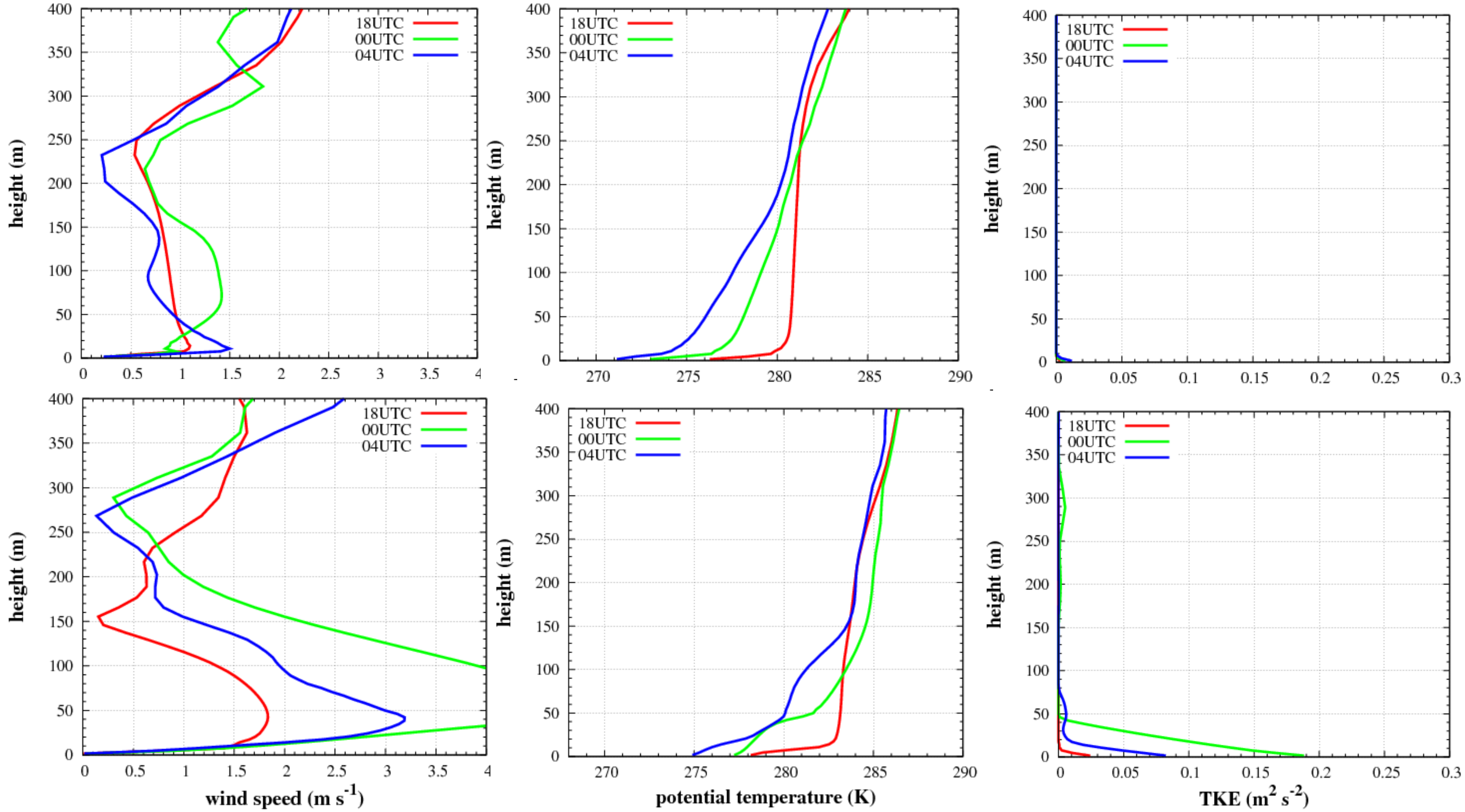

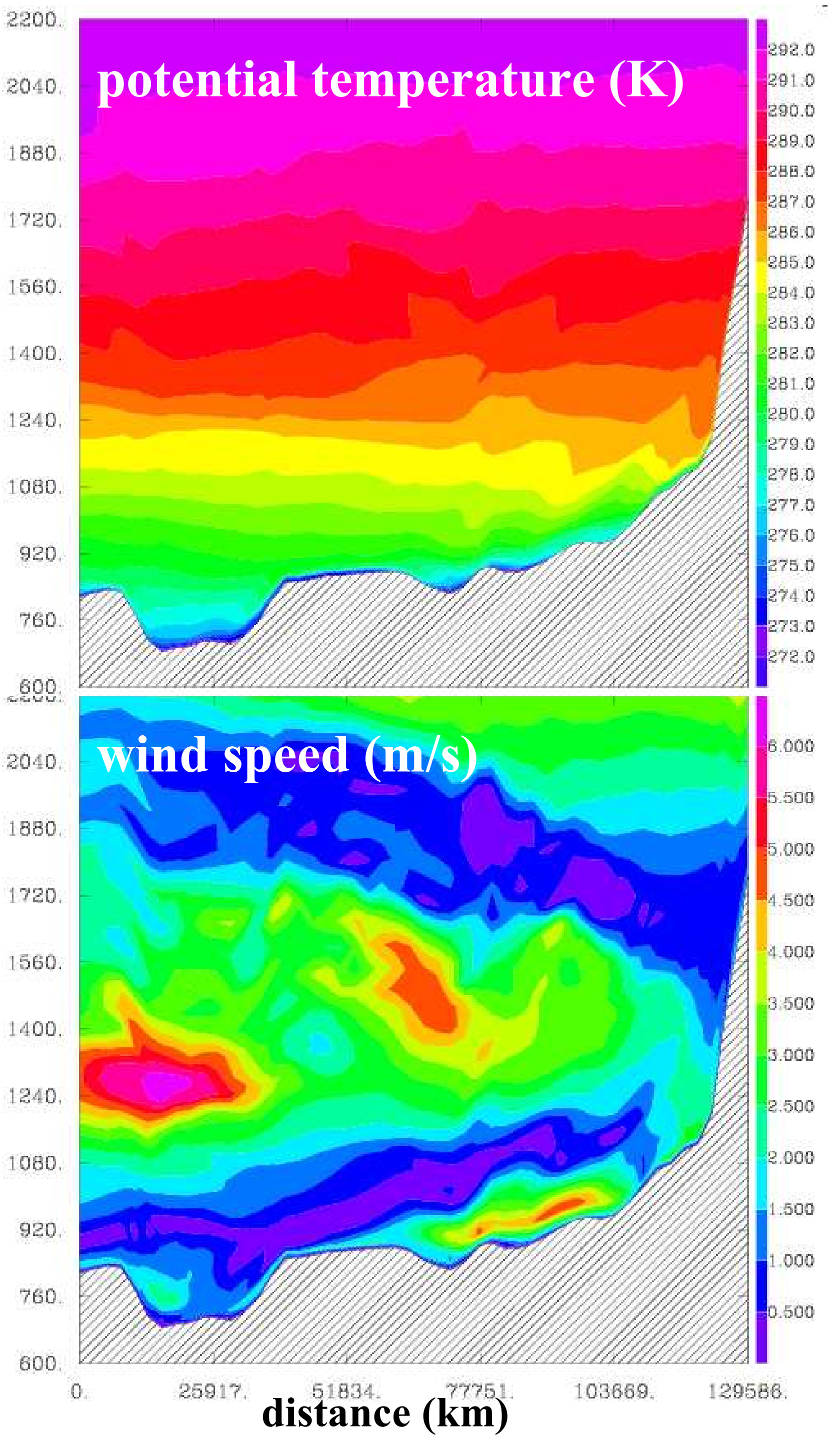

Katabatic flow obtained from the model at 0200 UTC

Cuxart et al. (2007)

Martínez and Cuxart (2009)

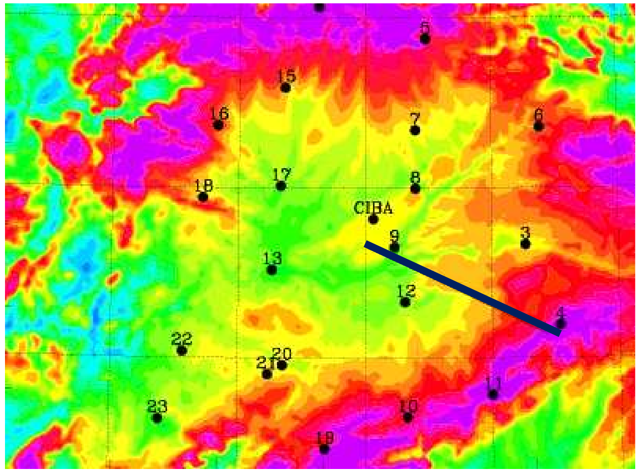

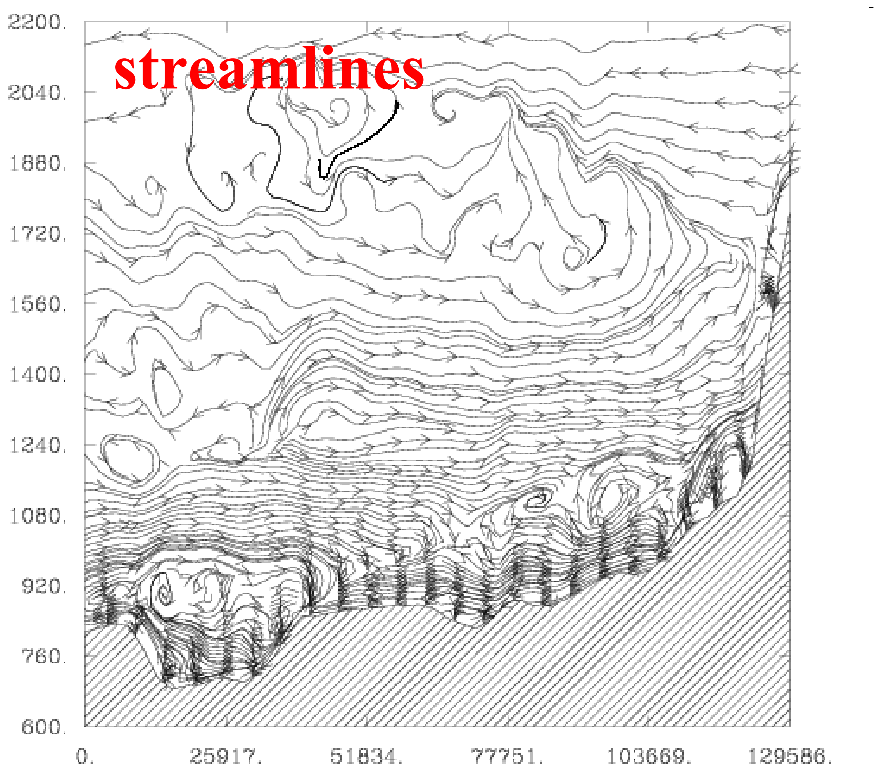

Hills, cliffs, holes…

Wavelength of an internal oscillation: $2\pi V / N_{BV}$
Length or height of the obstacle L, wavelength $2L$
Ratio: Froude Number: $Fr = \pi V / N_{BV} L$ (also described as the ratio between buoyant and inertial forces)

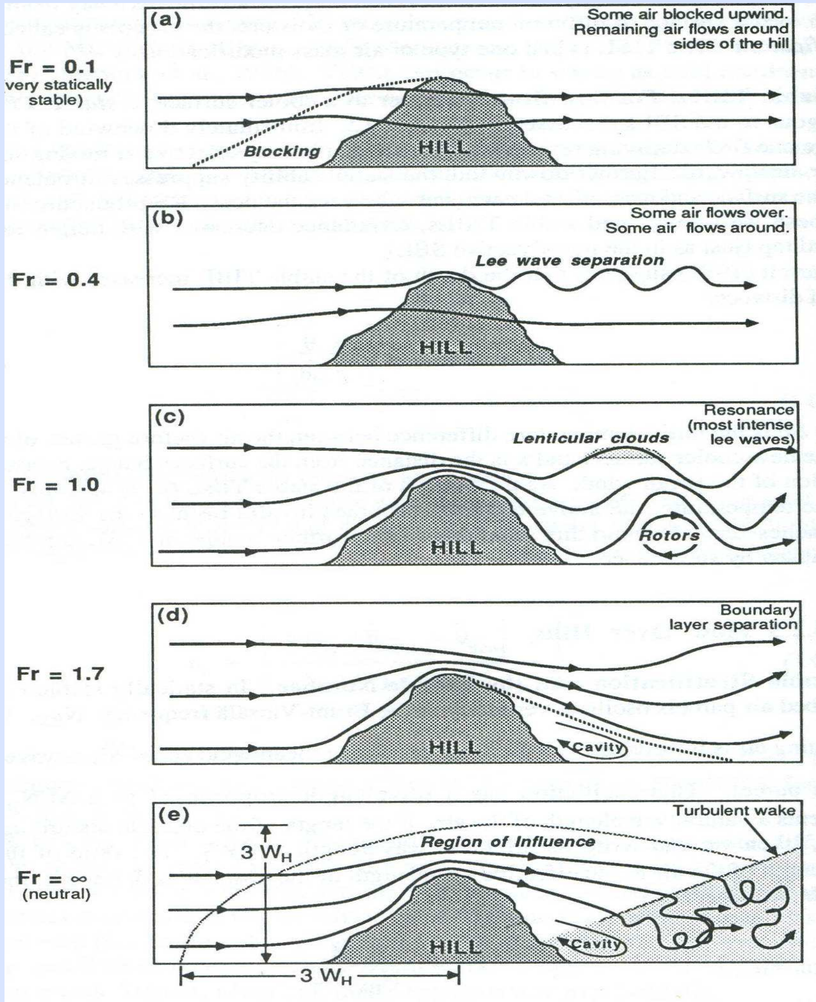

Fig. 14.14 Idealized flow over an isolated hill. The Froude number (Fr) compares the natural wavelength of the air to the width of the hill (W_H).

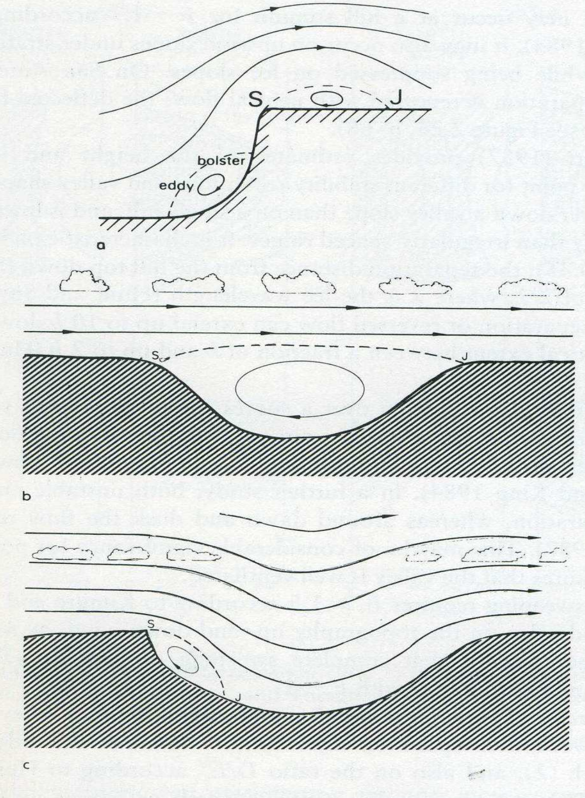

Figure 2.28 Examples of flow separation

(*a*) Separation at a cliff top (S), joining at J. A 'bolster' eddy resulting from flow divergence is shown at the base of the steep windward slope; (*b*) Separation on a lee slope with a valley eddy. The upper flow is unaffected; (*c*) Separation with a small lee slope eddy. A deep broad valley may cause the air to sink resulting in cloud dissipation above it.

Source From Scorer 1978

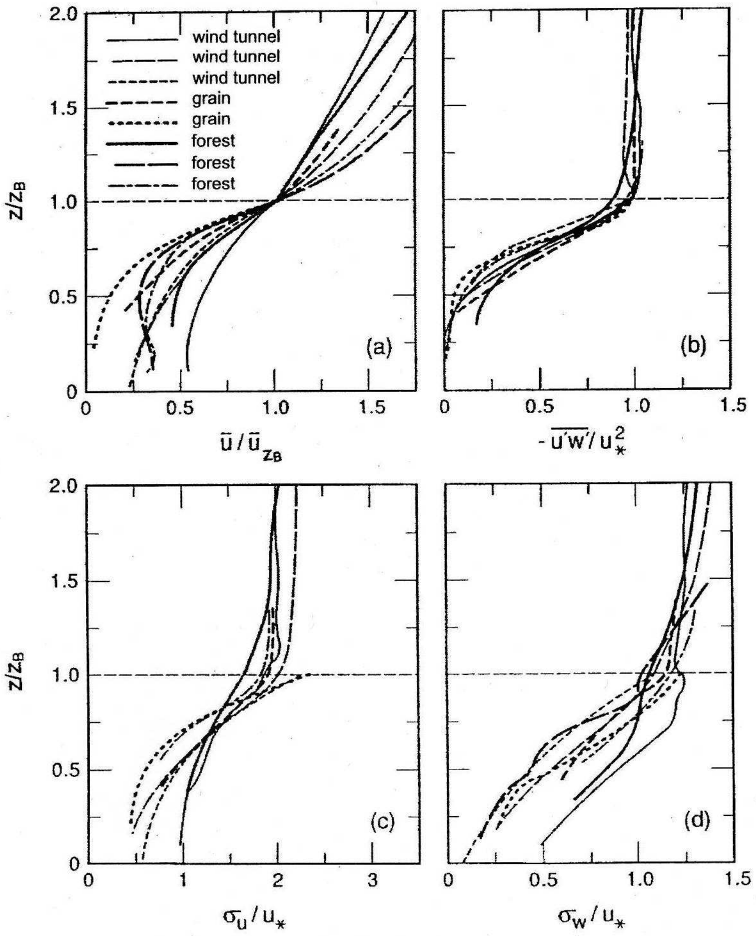

Fig. 3.6. Profiles of the mean wind velocity, the friction velocity and the standard deviations of the horizontal and vertical wind velocity normalized with their values at the canopy height according to different authors (Kaimal and Finnigan 1994)

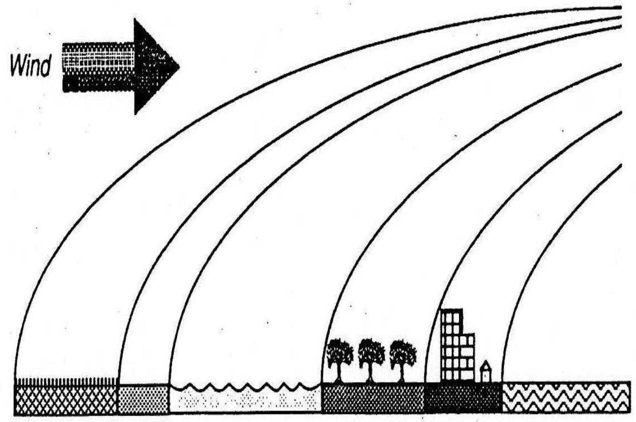

Fig. 3.7. Generation of internal boundary layers above an inhomogeneous surface (Stull 1988)

Radiation (weak and moderate wind)

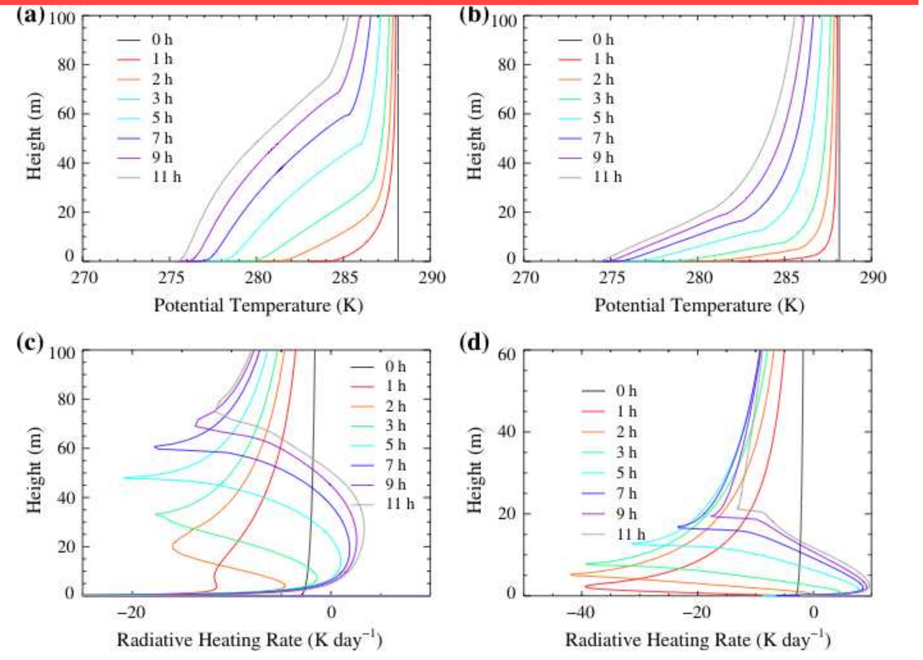

Fig. 4 Vertical profiles of potential temperature and radiative heating rates at hourly and subsequently two-hourly intervals. **a** Potential temperatures for a geostrophic wind of 7 m s^{-1}. **b** Potential temperatures for a geostrophic wind of 3 m s^{-1}. **c** Radiative heating rates for a geostrophic wind of 7 m s^{-1}. **d** Radiative heating rates for a geostrophic wind of 3 m s^{-1}

Fig. 10 **a** The radiative (*broken lines*) and turbulent (*solid lines*) heating rates at 2, 4 and 8 m for a geostrophic winds of 3 m s^{-1}. **b** As (**a**), but for a geostrophic wind of 1 m s^{-1}. **c** The surface temperature and the potential temperatures at 2 and 10 m for a geostrophic wind of 1 m s^{-1} (*solid lines*), together with the potential temperature at 2 m as inferred from conditions at the surface and at 10 m using surface similarity theory

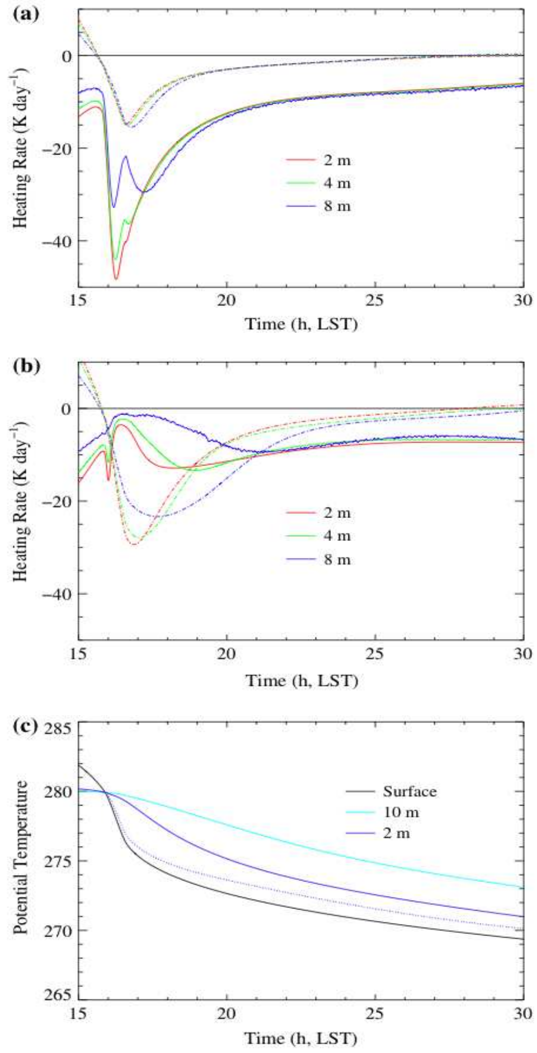

Edwards (2009)